VALIDATION AND APPLICATION OF A FIRST PRINCIPLE FLOTATION MODEL

KAIWU HUANG

Thesis submitted to the faculty of

Virginia Polytechnic Institute and State University

in partial fulfillment of the requirements for the degree of

MASTER OF SCIENCE

IN

MINING AND MINERALS ENGINEERING

ROE-HOAN YOON, CHAIR

GERALD H. LUTTRELL

GREGORY T. ADEL

August 5, 2015

Blacksburg, Virginia

Keywords: Flotation model, Flotation kinetics, Surface liberation, Bubble coarsening

VALIDATION AND APPLICATION OF A FIRST PRINCIPLE FLOTATION MODEL

KAIWU HUANG

ABSTRACT

A first principle flotation model has been derived from the basic mechanisms involved in the bubble-particle and bubble-bubble interactions occurring in flotation. It is a kinetic model based on the premise that the energy barrier (E_1) for bubble-particle interaction can be reduced by increasing the kinetic energy (E_k) for bubble-particle interaction and by increasing the hydrophobic force in wetting films. The former is controlled by energy dissipation rate (ε), while the latter is controlled by collector additions. The model consists of a series of analytical equations to describe bubble generation, bubble-particle collision, attachment and detachment, froth recovery, and bubble coalescence in froth phase. Unlike other flotation models that do not consider role of hydrophobic force in flotation, the first principle model developed at Virginia Tech can predict flotation recoveries and grades from the chemistry parameters such as ζ-potentials, surface tension (γ), and contact angles (θ) that may represent the most critical parameters to control to achieve high degrees of separation efficiencies.

The objectives of the present work are to i) validate the flotation model using the experimental data published in the literature, ii) incorporate a froth model that can predict bubble coarsening due to coalescence in the absence of particles, iii) develop a computer simulator for a froth model that can predict bubble coarsening in the presence of particles, and iv) study the effects of incorporating a regrinding mill and using a stronger collector in a large copper flotation circuit.

The model validation has been made using the size-by-class flotation rate constants (k_{ij}) obtained from laboratory and pilot-scale flotation tests. Model predictions are in good agreement with the experimental data. It has been found that the flotation rate constants obtained for composite particles can be normalized by those for fully liberated particles (k_{max}), which opens the door for minimizing the number of flotation products that need to be analyzed using a costly and time-consuming liberation analyzer.

A bubble coarsening froth model has been incorporated into the flotation model to predict flotation more accurately. The model has a limitation, however, in that it cannot predict bubble-coarsening in the presence of particles. Therefore, a new computer simulator has been developed to predict the effects of particle size and particle hydrophobicity on bubble coarsening in froth phase. In addition, the first principle flotation model has been used to simulate flotation circuits that are similar to the Escondida copper flotation plant to study the effects of incorporating a re-grinding mill and using a more powerful collector to improve copper recovery. The flotation model developed from first principles is useful for predicting and diagnosing the performance of flotation plants under different circuit arrangements and chemical conditions.

ACKNOWLEDGEMENT

My most sincere thanks go to my advisor, Dr. Roe-Hoan Yoon, who introduced me to the wonders and frustrations of scientific research. I thank him for his guidance, encouragement and support throughout this project. I would also like to thank Dr. Gerald Luttrell for his great help in dealing with problems in Excel-VBA. Finally, I would like to thank Dr. Greg Adel for serving on my committee.

I would like to express my deepest appreciation to Professor Jean-Paul Franzidis, SA Research Chair, Department of Chemical Engineering, University of Cape Town, South Africa, for his permission to use the size-by-class flotation rate constants and liberation data presented in the Ph.D. thesis authored by his former student Dr. Simon Welsby at the University of Queensland, Australia. I would also like to express my appreciation to Dr. Jaakko Leppinen, Technology Director – Mineral Processing, Outotec, for providing experimentally determined flotation rate constants along with relevant liberation data.

I am also grateful to FLSmidth for funding continuously for this project.

I also want to express my sincere gratitude to Dr. Lei Pan, Dr. Seungwoo Park, Dr. Juan Ma, Dr. Aaron Noble, Gaurav Soni, Zhenbo Xia, and Biao Li for helping me from time to time by giving me valuable advice.

Finally, I would like to express my eternal gratitude to my parents for their everlasting support and love.

Table of Contents

List of Figures

List of Tables

Nomenclature and Symbols[1]

DLVO- Derjaguin and Landau, Verwey and Overbeek
MIBC- Methyl Isobutyl Carbinol
a & b- Fitting parameters in the normalized rate constant (k/k_{max}) model
A- Cross-sectional area of the plateau border
A_b- Plateau border area at the bottom of a foam
A_{cr}- Critical rupture PB area
A_t- Plateau border area at the top of a foam
A_{232}- Hamaker constant for van der Waals interaction between two air/water interfaces
b_i- Fitting parameters in the contact angle calculation
C- Fitting parameter in the bubble coarsening foam model
C_{el}- Electrolyte concentration
d_1- Particle diameter
d_2- Bubble diameter
d_{12}- Collision diameter
$d_{2,b}$- Diameter of bubbles entering the froth phase
$d_{2,t}$- Diameter of bubble at the top of froth phase
e- Electronic charge
E_1- Energy barrier
E_k- Kinetic energy of attachment
E'_k- Kinetic energy of detachment
g- Gravitational acceleration constant
ΔG- Change of Gibbs free energy
h_f- Froth height
H- Thin liquid film thickness
H_{cr}- Critical rupture thickness
H_m- Medium thickness of a thin liquid film
H_0- The closest separation distance between two bubble surfaces
k- Overall flotation rate constant
k_{max}- Overall rate constant for the fully-liberated particles
k_p- Flotation rate constant in the pulp phase
k'- Boltzmann's constant
K_{132}- Hydrophobic force constant between bubble and particle
K_{131}- Hydrophobic force constant between two particles
K_{232}- Hydrophobic force constant between two bubbles
L- Rate constant ratio
m_1- Mass of the particle
m_2- Mass of the bubble
n- Number of flotation cells
N_0- Number of plateau borders at the base of a foam

[1] Symbols in red are the fitting parameters in the model.

N_1- Number of the particles
N_2- Number of the bubbles
N_{pb}- Number of the plateau borders
$N_{rupture}$- Number of films that rupture in the bubble coalescence process
p_c- Capillary pressure
P- Flotation probability
P_a- Probability of attachment
P_c- Probability of collision
P_d- Probability of detachment
P_f- Probability of bubble-particle aggregate surviving the froth phase
P_t- Probability of bubble-particle aggregates transferring from the pulp to the froth
r_1- Radius of the particle
r_2- Radius of the bubble
R- Overall flotation recovery
R_e- Froth recovery due to entrainment
R_p- Pulp phase recovery
R_f- Froth phase recovery
R_{film}- Film radius
R_{max}- Maximum fraction of the particles entering the froth phase
R_w- Maximum theoretical water recovery
R'- Gas constant
Re- Reynolds number
S_b- Bubble surface area flux
t- Retention time
t_{cr}- Critical rupture time of the thin liquid film
t_d- Drainage time
T- Absolute temperature
$\bar{u}_1$- Particle RMS velocity
$\bar{u}_2$- Bubble RMS velocity
U- Liquid drainage velocity
U_1- Radial velocity of the particle approaching a bubble
U_{Hc}- Velocity of a particle approaching a bubble at the critical rupture distance
V_D- van der Waals interaction energy
V_E- Electrostatic interaction energy
V_H- Hydrophobic interaction energy
V_g- Superficial gas rate
W_a- Work of adhesion
x- Fractional surface liberation
Z_{12}- Collision frequency between particles and bubbles
α- Fitting parameter in froth recovery calculation
β- Drag coefficient
ε- Energy dissipation rate
ε_b- Energy dissipation rate at bubble generation zone
ε_b'- Liquid fraction at the base of a foam (or froth)

ψ_s- Surface potential at the air/water interfaces
κ- Reciprocal of Debye length
γ_{lv}- Interfacial tension
μ- Dynamic viscosity
Π- Disjoining pressure
Π_{el}- Disjoining pressure due to electrostatic force
Π_{vw}- Disjoining pressure due to van der Waals dispersion force
Π_{hp}- Disjoining pressure due to hydrophobic force
ρ_1- Particle density
ρ_2- Bubble density
ρ_3- Medium density
τ_f- Retention time of air in the froth
θ- Contact angle
ν- Kinematic viscosity of the pulp
ζ- Zeta-potential

Chapter 1: INTRODUCTION

1.1 Background

1.1.1 Flotation History and Application

Flotation is undoubtedly the most important and versatile industrial process for the separation and concentration of minerals [1]. It is an amazing separation process that enables minerals denser than water to float to the top as bubble-particle aggregates for collection. This is achieved by exploiting the differences in surface properties between valuable minerals and gangue.

In 1860, the first hint that minerals can be separated from each other according to the differences in their surface properties appeared in a patent awarded to William Haynes [2], who claimed that sulfides could be floated by oil and non-sulfide minerals could be removed by washing in a powdered ore.

Bessel brothers built the first commercial flotation plant in Dresden, Germany, which was used to purify the graphite ore. The CO_2 bubbles were applied in their plant, which were generated by the reaction of lime with acid. The first flotation plant to process sulfide ores was based on Carrie Everson's patent. The year 1885 was important in the flotation history due to the patents by the Bessel brothers and Carrie Everson.

True industrialization of the flotation process, from being a research topic in the lab to a more commercially valuable tool, occurred in the early twentieth century [3]. In 1901, the immediate problem occurred at Broken Hill, Australia, which was finding a way to recover sphalerite fines from the waste dumps. Several flotation processes and machines were studied there by engineers in different programs. The results of these programs were that froth flotation was developed as an industrial process for concentrating sulfides and was used to recover zinc from millions of tons of slime tailings.

Froth flotation was used in the United States for the first time in 1911. The first flotation plant in the US was installed by James M. Hyde in Basin, Montana [4], who understood and verified that the use of rougher-cleaner closed circuits could remove entrained gangue particles from concentrates. The success of this plant was a milestone which represented flotation was poised to take off [5].

During 1925-1960, the introduction of chemical reagents and the trend of selective flotation brought about more widespread application of flotation process as an economic tool. To meet the increased demand for minerals by flotation, the capacity of flotation plant increased a lot. In the following decades, with the improvement of flotation cells and development of on-stream analysis (OSA) systems, the mineral production from flotation increased rapidly and accurate control of flotation circuits was achieved.

Over the past decades, flotation has been used not only in the mineral processing industries, but also in the food industries, *e.g.*, removing solids in butter and cheese. It is also commonly used for removing the contaminant from water so that purification can be achieved. Other areas in which flotation can be applied are de-inking of recycling paper, paint manufacturing, and paper industry [5].

The flotation process as it exists today remains essentially the same as it was in Broken Hill [6]. A feed of slurry is pre-treated with suitable reagents in a tank where it is agitated to keep the solids in suspension before being pumped into a series of flotation cells. In the flotation cell, the slurry is agitated by an impeller, where air is also injected to generate fine bubbles. As bubbles rise in the slurry, they collect hydrophobic particles selectively and enter the froth phase on the top. The forth laden with hydrophobic particles overflows the cell lip and recovered as a concentrate.

1.1.2 Flotation Process

Flotation is a process for separating finely divided solids from each other using air bubbles under hydrodynamic environment. The process is based on separating hydrophilic particles from hydrophobic ones in the slurry by attaching the latter selectively onto the air bubble surfaces [3]. Specific chemicals, which are known as collectors, are added to the slurry before flotation to increase the differences in hydrophobicity of the minerals to be separated. In general, the recovery and selectivity of flotation increases with increasing hydrophobicity difference.

Thermodynamically, for bubble-particle attachment to occur, the change of Gibbs free energy (ΔG) must be less than zero. The changes of free energy in bubble-particle attachment can be described as the changes in the interfacial tensions at the solid-liquid, solid-air and air-liquid interfaces [7]. By applying Young's equation, one can obtain the following relationship for the change of Gibbs free energy,

$$\Delta G = \gamma_{lv}\left(\cos\theta - 1\right) \tag{1}$$

where γ_{lv} is the interfacial tension and θ is the contact angle at the three phase contact point. Eq. (1) shows that $\Delta G < 0$ when $\theta > 0$, and that the higher the contact angle, the more negative ΔG becomes.

Bubble-particle aggregates rise through the pulp since the overall density of the aggregates are lower than the density of the slurry. At the pulp/froth interface, some of the air bubbles loaded with various particles enter the froth phase, while others may drop off depending on the bubble size, particle size, and bubble loading. Froth is a complex three-phase system, which contains air bubbles, particles, and liquid films. At the bottom of a froth phase, bubbles are separated by thick water films. The liquid films become thinner as the bubbles rise in the froth phase, creating thin liquid films (TLFs) (or lamellae films). Three lamellae films meet at a plateau border (PB), through which water drains. As the thickness of the lamella film between two bubbles reach a critical thickness (H_{cr}), the TLF ruptures and two bubbles become one,

which is referred to as *bubble coarsening.* As bubbles become larger, the surface area on which hydrophobic particles are attached (or 'parked') become smaller, forcing less hydrophobic particles to detach and return to the pulp phase [8]. Thus, the bubble coarsening provides a mechanism by which product grade improves.

Two mechanisms, *i.e.*, recovery due to attachment and recovery due to entrainment, contribute to the recovery in froth phase. The former represents true recovery based on hydrophobic interactions, while the latter represents unwanted recoveries due to hydraulic entrainment associated with the recovery of water or water split [9]. Fine particles with low inertia are prone to the hydraulic entrainment.

1.1.3 Role of Modeling Flotation

Flotation is a complex physiochemical process involving solid, liquid, and gas phases; therefore, the number of parameters affecting the process is large. These parameters can be subdivided broadly into two groups, *i.e.*, hydrodynamic and surface chemistry parameters. The former includes particle size, bubble size, energy dissipation rate, *etc*., while the latter includes contact angle (θ), ζ-potential, Hamaker constants, and surface tension (γ). Many investigators developed flotation models in the past, most of which are based on the hydrodynamic parameters. On the other hand, the separation efficiencies of flotation are determined by control of surface chemistry parameters rather than hydrodynamic parameters, particularly the hydrophobicity of the particles to be separated, as has already been noted in the foregoing section. For this reason, Virginia Tech has been developing a flotation model using both the hydrodynamic and surface force parameters. The first principle model can, therefore, predict both the recovery and grade for the first time.

Having a first principle model has many advantages, the most important aspects including predictive and diagnostic capabilities. There are some parameters that are difficult to be tested in experiment without affecting other parameters. For example, changing the pH to study the effect of ζ-potentials of particles also affect the ζ-potentials of air bubbles as well as the collector adsorption and hence the particle contact angles. A first principle model can easily study the effects of isolated process variables one at a time and, thereby, optimize a flotation circuit. In addition, the model-based simulator can be used design flotation plants with minimal input from experiment.

1.2 Literature Review

1.2.1 Flotation Modeling

Flotation is a 3-phase separation process. Therefore, modelling flotation is difficult simply because of the large number of parameters involved. Furthermore, a bubble-particle interaction involves several different sub processes, which need to be modeled separately. A large number of factors and interactions between them need to be considered in the flotation model, since all of these can affect the flotation results in different ways.

Currently, there are several academic or commercial flotation models and simulators to predict the performance of flotation circuits or a flotation unit, such as the P9 Flotation Model, limn, USIM PAC simulator and SUPASIM flotation simulation program.

The P9 Flotation Model has been developed at the Julius Kruttschnitt Mineral Research Center (JKMRC) over the past twenty years [6]. Both entrainment and true flotation are considered when it comes to simulating the recovery of particles. The recovery is given as [10]:

$$R_{i,j} = \frac{\left(P_{i,j} S_b R_{fi,j} \tau\right)\left(1 - R_w\right) + ENT_i R_w}{\left(1 + P_{i,j} S_b R_{fi,j} \tau\right)\left(1 - R_w\right) + ENT_i R_w} \tag{2}$$

where subscript *i* represents a particle size class, and subscript *j* represents a surface liberation class. *P* is ore floatability, *R* is overall recovery, τ is residence time, R_w is water recovery, S_b is the bubble surface area flux in the pulp zone and *ENT* is degree of entrainment.

Drawback of this model is that the parameters used in the model must be acquired from flotation tests data and surveying. Therefore, the collection of representative samples and good experimental data can determine that whether a simulation of a flotation circuit/unit is a successful one or not.

Limn software is an Excel-based application that allows the user to draw and model a circuit. Limn software incorporates partition models for gravity separation and size separation, which is powerful in stream simulation. In the Limn, however, the flotation recovery is also simulated by the partition model, in which the *Ep* and *Rho50* values are entered manually to fit the yield and grade data from the flotation tests. The lack of effective flotation model is the main disadvantage of the Limn software.

SUPASIM flotation simulation model was developed in the mid-1980s by Eurus Mineral Consultants to predict plant performance from standard laboratory flotation tests [11]. The model is based on Kelsall's unmodified equation in which two rate constants appear,

$$R = (100 - \Theta)\left[1 - \exp\left(-k_f t\right)\right] + \Theta\left[1 - \exp\left(-k_s t\right)\right] \tag{3}$$

where Θ is slow floating fraction, *t* is flotation time, *R* is percentage recovery at time *t*, k_f is fast floating rate constant and k_s is slow floating rate constant. Θ, k_f, and k_s are estimated from the laboratory batch flotation tests. Based on these parameters, the continuous flotation process can be modelled by applying the scale-up algorithms.

USIM PAC simulator is an easy to use steady-state simulation software developed by BRGM since 1986 [12]. It contains several flotation models which can be classified as "performance" models and "predictive" models [13]. Performance models are made for material balance calculation and definition, while predictive models are based on kinetic approach.

A Model with two kinetic rate constants considers that the feed is composed of three "sub-populations", non-floating, fast floating and slow floating. Assuming that each cell is represented as a perfectly mixed reactor, flotation can be described as,

$$F_{fj} = F_j R\inf_j \left[\varphi_j \left(1 - \frac{1}{1+ks_j\tau} \right) + (1-\varphi_j)\left(1 - \frac{1}{1+kf_j\tau} \right) \right] \quad (4)$$

where F_{fj} is flow rate of mineral j in the froth, F_j is flow rate of mineral j in the feed, $Rinf_j$ is maximum possible recovery of j in the froth, φ_j is proportion of mineral j capable of floating and which shows slow floating behavior, and τ is mean residence time.

Another predictive model incorporates a distribution of kinetic constants according to particle size. The kinetic rate constant is calculated for each mineral j and each size class i as below,

$$k_{i,j} = \frac{\alpha}{x_i^{0.5}} \left[1 - \left(\frac{x_i}{xl_j} \right)^{1.5} \right] \exp\left[-\left(\frac{xe_j}{2x_i} \right)^2 \right] \quad (5)$$

where x_i is average size in size fraction i, α_j is adjustment parameter for mineral j, xl_j is the largest floating particle size for mineral j, and xe_j is the easiest floating particle size for mineral j. In perfectly mixed condition, flotation can be described as,

$$Ff_{i,j} = F_{i,j} R\inf \left(1 - \frac{1}{1+k_{i,j}\tau} \right) \quad (6)$$

where $Ffi_{,j}$ is flow rate of mineral j and size class i in the froth and Fi,j is flow rate of mineral j and size class i in the feed.

USIM PAC also includes an entrainment model, which is based on the reference [14]. Recovery due to entrainment is shown below,

$$R_{i,j} = P_{i,j} R_w \quad (7)$$

where $P_{i,j}$ is recovery of mineral j in size class i in one cell and R_w is water recovery.

The flotation models or simulators mentioned above all require basic input data from flotation tests, which causes the limitation of applying these models to predict flotation performance. However, the flotation model developed from first principles helps better understand and predict flotation process. A flotation model considering both surface chemistry parameters and hydrodynamic conditions was first proposed by Yoon and Mao, 1996. The model was further improved by other researchers at the Center for Advanced Separation Technologies

at Virginia Tech [3, 15, 16]. The first principle flotation model will be presented in the following chapter.

1.3 Research Objectives

The objectives of the present research are to verify and to improve the first principle flotation model developed at Virginia Tech. The main focus of the improvement will be to incorporate the bubble coarsening model to the model, so that it can predict bubble size ratio in the froth phase. To validate the model and simulator, the results of a series of flotation tests conducted by other researchers and reported in the literature will be used as data base for model verification and simulation using the first principle flotation model. The model parameters will be adjusted so that the model prediction and simulation results will be in close agreement with the flotation test results. Once the model has been verified, the computer simulator based on the first-principle model will be used to predict the effects of various parameters that are critically important in industry. The parameters to be studied will include particle size, degree of mineral (or surface) liberation, circuit arrangement, and others.

1.4 Organization

The body of this thesis consists of five chapters:

Chapter 1 provides background information of flotation and flotation modeling. Several flotation models or simulators are introduced in this chapter that have been developed and applied in the mineral processing industry. This chapter also introduces the research objective of the present work.

Chapter 2 presents the model equations for flotation and bubble coarsening in froth phase. The models are developed from first principles, which can help understand the various sub processes occurring in flotation.

Chapter 3 presents the results of model validation. A computer simulator is used to validate the model against the results of a series of pilot-scale continuous flotation tests reported in the literature and against a laboratory-scale flotation tests.

Chapter 4 presents the simulation results without experimental validation. The flotation model is used to study the effects of various process parameters such as particle size, contact angle, forth height, ζ-potential and others. Furthermore, the simulator is used to see the effect of changing flotation circuits as a means for optimization.

Chapter 5 summarizes the results of the work presented in the foregoing chapters and suggests future work.

Chapter 2: FLOTATION MODEL BASED ON FIRST PRINCIPLES

2.1 Framework

2.1.1 Pulp Phase Recovery

Flotation Kinetics

Flotation process can be modeled as a first-order rate equation [17, 18],

$$\frac{dN_1}{dt} = -kN_1 \tag{8}$$

in which k is the rate constant and N_1 is number of particles in a cell. Under a steady condition, k can be determined by [19],

$$k = \frac{1}{4} S_b P \tag{9}$$

where P is probability of flotation and S_b is bubble surface area flux.

Generally, P is composed of four parts as shown below,

$$P = P_a P_c (1 - P_d) P_t \tag{10}$$

where P_a represents the probability of attachment, P_c the collision probability, P_d the probability of detachment in pulp phase, and P_t represents the probability of bubble-particle transfer at the pulp-froth interface.

In the past, flotation processes were often modeled as a first-order process with a single rate constant for the sub-processes of pulp and froth phase recoveries, which is overall rate constant (k). In the current model, however, the two sub-processes are considered separately and subsequently combined to obtain an overall flotation rate.

Basically, flotation process should be considered a second-order process in that its rate should depend on concentration of particles (N_1) and bubbles (N_2). If one assumes $N_2 >> N_1$ or N_2 remains constant during flotation, the process may be considered a pseudo first-order process and may be represented as

$$\frac{dN_1}{dt} = -k_p N_1 = -Z_{12} P \tag{11}$$

where k_p is the rate constant in the pulp phase, and Z_{12} is the collision frequency. Z_{12} can be calculated as below [20],

$$Z_{12} = 2^{3/2}\pi^{1/2} N_1 N_2 d_{12}^2 \sqrt{\bar{u}_1^2 + \bar{u}_2^2} \tag{12}$$

which was derived originally by Abramson [21] based on the assumption that particle velocities were independent of fluid flow. In Eq. (12), d_{12} is the collision diameter (sum of radii of bubbles and particles), and $\bar{u}_1$ and $\bar{u}_2$ are the root-mean-square (RMS) velocities of the particles and bubbles, respectively. Substituting Eq. (11) into Eq. (12), one can obtain,

$$\frac{dN_1}{dt} = -2^{3/2}\pi^{1/2} N_1 N_2 d_{12}^2 \sqrt{\bar{u}_1^2 + \bar{u}_2^2}\, P \tag{13}$$

From Eqs. (11) and (13), one can obtain,

$$k_p = \frac{Z_{12} P}{N_1} \tag{14}$$

Bubble Generation Model

The diameters of bubbles (d_2) were calculated using the bubble generation model derived by Schulze [22],

$$d_2 = \left(\frac{2.11\gamma_{lv}}{\rho_3 \varepsilon_b^{0.66}} \right)^{0.6} \tag{15}$$

where γ_{lv} is the surface tension of the water in a flotation cell, ρ_3 is the density of the water, and ε_b is the energy dissipation rate in the bubble generation zone. In the present work, it is assumed that air bubbles are generated at the high energy dissipation zone in and around the rotor/stator assembly, which has 15-times larger energy dissipation rate than the mean energy dissipation rate (ε) of a flotation cell [22].

RMS Velocities

The RMS velocity of the particles is calculated using the following empirical relation [20],

$$\bar{u}_1 = 0.4 \frac{\varepsilon^{4/9} d_1^{7/9}}{\upsilon^{1/3}} \left(\frac{\rho_1 - \rho_3}{\rho_3} \right)^{2/3} \tag{16}$$

where ε is energy dissipation rate, d_1 particle diameter, v kinematic viscosity of water, ρ_1 is particle density, and ρ_3 is the density of water.

On the other hand, the RMS velocity for bubbles is calculated using the following equation [23],

$$\bar{u}_2 = \left(C_0 (\varepsilon d_2)^{2/3}\right)^{1/2} \tag{17}$$

where C_0 (= 2) is a constant and d_2 is bubble diameter.

Flotation Probability

a) Probability of Attachment (P_a)

In calculating flotation probability, P, the probability of attachment is given by [19]

$$P_a = \exp\left(\frac{-E_1}{E_k}\right) \tag{18}$$

where E_1 is the energy barrier and E_k is the kinetic energy available during attachment process.

The value of E_1 can be determined using extended DLVO theory [24, 25],

$$E_1 = V_E + V_D + V_H \tag{19}$$

where V_E, V_D and V_H are the bubble-particle interaction energies due to electrostatic, van der Waals and hydrophobic forces, respectively. In the present model, V_E is calculated using the HHF model [26], while V_D is calculated using the van der Waals equation [27]. The interaction energy due to the hydrophobic force is determined using following relation,

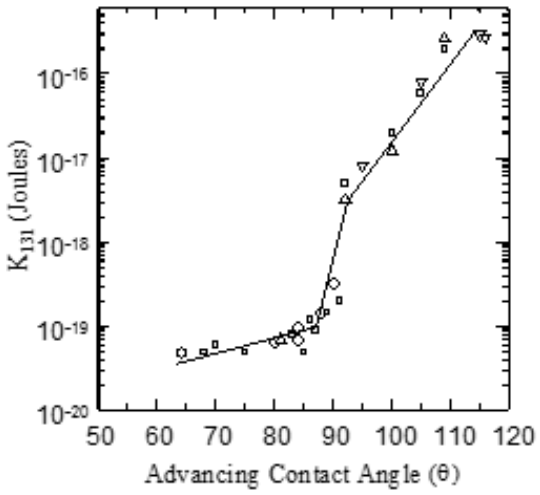

Figure 2.1: Relationship between K_{131} and advancing contact angle of particle (θ).

$$V_H = -\frac{K_{132} r_1 r_2}{6H_0(r_1 + r_2)} \tag{20}$$

where H_0 is the closest separation distance between bubble of radius r_2 and particle of radius r_1 in water, and K_{132} is the hydrophobic force constant between the bubble and the particle [27]. It has been shown that hydrophobic interaction between hydrophobic solid surface and bubble surface with different contact angles can be predicted using the combining law [19],

$$K_{132} = \sqrt{K_{131} K_{232}} \tag{21}$$

where K_{131} is the hydrophobic force constant between two particles in a medium and K_{232} is the hydrophobic force constant between two air bubbles in a medium [28]. Figure 2.1 [29] shows the relationship between K_{131} and particle advancing contact angle, from which one can clearly see that K_{131} increases with the increase of the contact angle. In the present work, the values of K_{131} has been determined using the data presented in Figure 2.1.

To calculate P_a using Eq. (18), it is necessary to know the value of E_k. The kinetic energy may be calculated using following relation,

$$E_k = 0.5 m_1 (U_{Hc})^2 \tag{22}$$

where m_1 is the mass of the particle, and U_{Hc} is the velocity of the particle approaching a bubble surfaces at the critical rupture distance (H_c). In the present work, the following equation has been used to calculate U_{Hc},

$$U_{Hc} = U_1 / \beta \tag{23}$$

where U_1 is radial velocity of the particle approaching a bubble and β is the drag coefficient in the boundary layer of the bubble [30]. The values of U_1 and β have been determined as described previously [31],

b) Probability of Collision (P_c)

In the present work, Eq. (24) is used to determine the probability of collision, which is shown below,

$$P_c = \tanh^2\left(\sqrt{\frac{3}{2}\left[1 + \frac{3}{16}\left(\frac{Re}{1 + 0.249 Re^{0.56}}\right)\right]}\left(\frac{d_1}{d_2}\right)\right) \tag{24}$$

where d_1 and d_2 are bubble and particle diameters, respectively, and Re is the Reynolds number. Eq. (12) represents a hard-core collision model, that is, bubble-particle collision occurs when the two macroscopic spheres approach each other within the collision radius (r_{12}), which is effective only under extremely turbulent conditions. For quiescent flow, however, the collision is affected

by the streamlines around bubbles. The truth may lie in between. Therefore, one may get correct Z_{12} by multiplying P_c [31].

c) Probability of Detachment (P_d)

The probability of detachment is calculated using the following expression [19]

$$P_d = \exp\left(\frac{-W_a + E_1}{E_k^{'}}\right) \tag{25}$$

where W_a is the work of adhesion, and E_k' is the kinetic energy of detachment. W_a can be obtained from the following relation,

$$W_a = \gamma_{lv}\pi r_1^2 (1-\cos\theta)^2 \tag{26}$$

where γ_{lv} is the surface tension of water, r_1 is the radius of the particle, and θ is the contact angle.

By using Eq. (25), E_k' can be calculated using the following relation [15],

$$E_k^{'} = 0.5 m_1 \left((d_1 + d_2)\sqrt{\varepsilon/\upsilon}\right)^2 \tag{27}$$

where ε is the energy dissipation rate and ν is the kinematic viscosity.

Pulp Recovery Calculation

In a mechanically-agitated cell, the pulp phase recovery, R_p, can be calculated as below,

$$R_p = \frac{k_p t}{1 + k_p t} \tag{28}$$

in which k_p is the flotation rate constant in the pulp phase. Eq. (28) is applicable for perfectly mixed flotation cells as is the case with a mechanically-agitated individual cell in a flotation bank.

For plug-flow reactors, one may use the relation below to calculate R_p,

$$R_p = 1 - e^{-k_p t} \tag{29}$$

2.1.2 Froth Phase Recovery

It is well kwon that the forth recovery accounts for two independent mechanisms, *i.e.* recovery due to attachment and recovery due to entrainment. Fine particles are recovered by entrainment, while coarse and hydrophobic particles are recovered by attachment. Thus, the overall froth recovery (R_f) can be written as follows [16],

$$R_f = R_{\max} \exp\left(-\alpha \tau_f\right) + R_e \tag{30}$$

in which $R_{\max}$ is the maximum fraction of the particles entering the froth phase that is recovered into a launder, τ_f is the retention time of air in the froth, and R_e is the recovery of particles due to entrainment. Former researchers [15] have developed equations for calculating of R_e and τ_f. In addition, it can be readily seen that $R_{\max}$ should vary with bubble coalescence as follows,

$$R_{\max} = \frac{S_t}{S_b} = \frac{d_{2,b}}{d_{2,t}} \tag{31}$$

where S_t and S_b are the bubble surface areas on the top and bottom of a froth phase, respectively, while $d_{2,t}$ and $d_{2,b}$ are the bubble diameters at the top and bottom, respectively.

2.1.3 Overall Recovery

Figure 2.2 shows the diagram to calculate the overall flotation recovery [3], in which R_p is the recovery in the pulp phase and R_f is the recovery in the froth phase. According to the diagram, one can readily find that the overall recovery, R, can be calculated using the equation below,

$$R = \frac{R_p R_f}{R_p R_f + 1 - R_p} \tag{32}$$

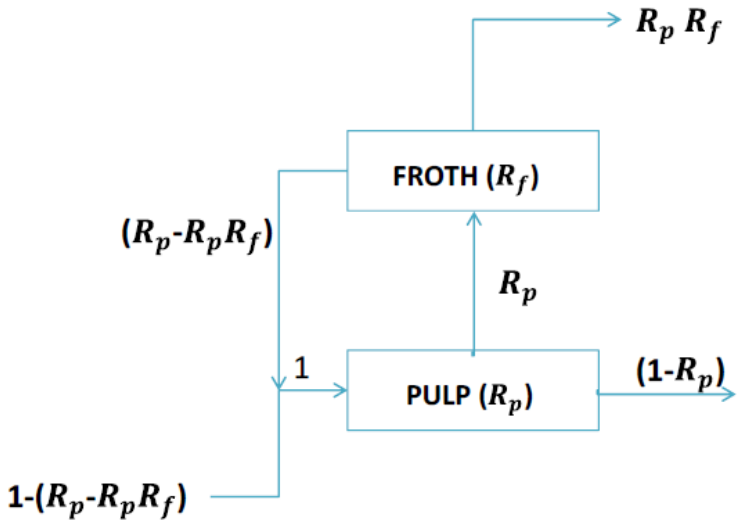

Figure 2.2: Diagram of mass balance of materials around a flotation cell. Soni, G., *Development and Validation of a Simulator based on a First-Principle Flotation Model*. 2013, Virginia Tech. Used under fair use, 2015.

Note here that one can calculate the overall rate constant (k) using the equation below under a perfectly mixed flotation cell,

$$k = k_p R_f \tag{33}$$

By combining Eqs. (28), (32) and (33), one can get the relationship between overall flotation rate constant (k) and overall flotation recovery (R),

$$kt = \frac{R}{1-R} \tag{34}$$

which is the same as the overall rate constant equation under perfectly mixed condition developed by Levenspiel [32].

2.2 Bubble Coarsening Model

In the flotation froth, air bubbles become larger and larger with the increase of froth height, which is due to bubble coalescence phenomenon. Bubble coalescence has significant impacts on the flotation recoveries and grades, as it causes the bubble surface area to decrease along the vertical direction, which forces some particles to drop back to the pulp phase. In the calculation of froth recovery due to attachment, one needs to determine R_{max}, which depends on the bubble size ratio ($d_{2,t}/d_{2,b}$). In the past, an assumed value of bubble size ratio was used in Eq. (31). At present, a bubble coarsening model has been incorporated in the current flotation model to predict the bubble size ratio accurately.

2.2.1 Bubble Coarsening Foam Model

In this section, a 2-phase bubble coarsening model will be introduced, which does not consider the effects of particle size and particle hydrophobicity on the stability of the froth. Therefore, the model to be described below may be applicable for foam rather than froth.

Eq. (35) describes the drainage of liquid in a foam,

$$U = \frac{1}{\mu}\left(\rho g A - \gamma \frac{1}{\sqrt{A}} \frac{\partial A}{\partial x}\right) \tag{35}$$

where U is the drainage rate; g is the gravitational acceleration; μ, ρ, and γ are the dynamic viscosity, density, and surface tension of water, respectively; A is the cross-sectional area of the plateau border (PB), and x is the distance from the top of the foam.

At a steady state, the downward liquid drainage velocity (U) should be equal to the upward superficial gas velocity ($-V_g$),

$$U = -V_g \tag{36}$$

Combining Eqs. (35) and (36) and then integrating from the top to the bottom of a foam, one can obtain,

$$\sqrt{A_t} = \sqrt{\frac{V_g \mu}{\rho g}} \tan\left[\tan^{-1}\left(\sqrt{\frac{\rho g A_b}{V_{g\mu}}} \right) \right] - \frac{h_f}{2} \frac{\sqrt{\rho g \mu V_g}}{\gamma} \tag{37}$$

where A_t and A_b are PB areas at the top and bottom of a foam, respectively, and h_f is the foam height.

In a dry foam, it is reasonable to assume that the number of PBs (N_{pb}) is proportional to the number of bubbles, which can be calculated by dividing the cross-sectional area (S) of a foam (or froth) column by bubble size, *i.e.*, $4s/\pi d^2$. One can then write the following relation,

$$\frac{N_{pb,t}}{N_{pb,b}} = \frac{4s/\pi d_{2,t}^2}{4s/\pi d_{2,b}^2} = \left(\frac{d_{2,b}}{d_{2,t}} \right)^2 \tag{38}$$

where $N_{pb,t}$ and $N_{pb,b}$ are the numbers of PB at the top and bottom of a foam, respectively, and $d_{2,t}$ and $d_{2,b}$ are the corresponding bubble sizes.

As a foam drains, A decreases with time, or the foam becomes drier. At the same time, the thickness (H) of the lamella films will also become thinner. As H becomes smaller, there will be a critical point where a lamellar film will rupture instantaneous, which is referred as critical rupture thickness of the liquid film (H_{cr}). Accordingly, it may be reasonable to suggest that bubbles begin to coalesce when A reaches A_{cr}. As bubbles coalesce, N_{pb} will decrease. In the present work, the changes of N_{pb} is represented by the following relation,

$$N_{pb} = N_0 \exp\left(-C \sqrt{\frac{A_{cr}}{A}} \right) \tag{39}$$

where N_0 is the number of PBs at the base of a foam, and C is an adjustable parameter. Eq. (39) shows that N_{pb} decreases exponentially with the square root of A_{cr}.

Substituting Eq. (39) into Eq. (38), one obtains the following relation,

$$\frac{d_{2,b}}{d_{2,t}} = \sqrt{\exp C \sqrt{A_{cr}} \left(\frac{1}{\sqrt{A_b}} - \frac{1}{\sqrt{A_t}} \right)} \tag{40}$$

which shows that bubble size ratio, or bubble coarsening, can be predicted if the values of A_b, A_t and A_{cr} are known.

According to Eq. (37), one can determine the value of A_t if A_b is known. One can calculate the values of A_b by considering the geometrical relationships between bubbles, lamellar films, and Plateau borders as follows [33, 34],

$$\sqrt{A_b} = 0.4\left(0.892 d_{2,b}\sqrt{\varepsilon_b^{'}}\right) \tag{41}$$

where $d_{2,b}$ is the bubble size at the base of a foam (or froth), which may be considered the same as the bubble size in the pulp phase; and $\varepsilon_b{}'$ is the liquid fraction at the base of the foam under consideration. One can then determine $d_{2,b}$ using a bubble generation model [22] and obtain $\varepsilon_b{}'$ using a drift-flux model[35].

In calculating the bubble size ratio using Eq. (40), it is necessary to know the value of A_{cr}. In this study, the values of A_{cr} were calculated from those of H_{cr} based on the geometric relation (Figure 2.3) between A_{cr} and H_{cr} [9], as follows,

$$A_{cr} = (\sqrt{3} - \frac{\pi}{2}) R_{pb}{}^2 + \sqrt{3} R_{pb} H_{cr} \tag{42}$$

where R_{pb} is the radius of curvature of PB.

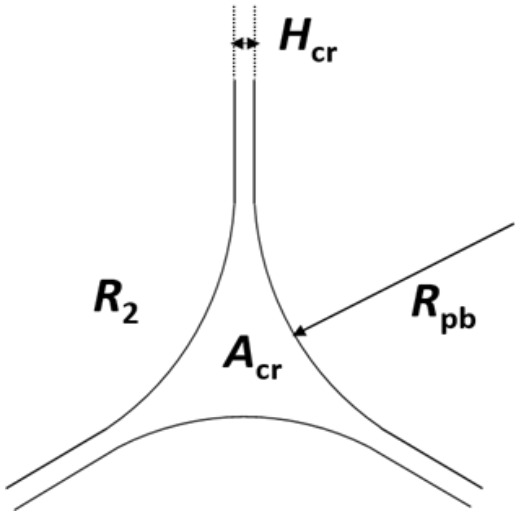

Figure 2.3: Plateau boarder area (A) in relation to critical lamella film thickness (H_{cr}), bubble size (R_2), and plateau boarder radius (R_{pb}) in a dry foam.

2.2.2 Bubble Coarsening Froth Model

In this section, a froth model evaluating bubble coalescence is presented, which is also developed from first principles by Park and Yoon [36]. The model considers the bubble size ratio as functions of particle size (d_1), particle hydrophobicity (contact angle), froth height (h_f), aeration rate (V_g) and surface tension (γ).

It is known that bubble coalescence occurs at the point when a thin liquid film (TLF) between two air bubbles breaks in the froth phase. The rate of film thinning can be analyzed using the Reynolds lubrication Equation [37],

$$\frac{dH}{dt_d} = \frac{2H^3 p}{3\mu R_{film}^2} \tag{43}$$

where H is the TLF thickness, t_d is drainage time, μ is dynamic viscosity, R_{film} is film radius and p is the driving force for the film thinning. The driving force for film thinning p is determined by the following relation,

$$p = p_c - \Pi \tag{44}$$

which shows that the driving force is the sum of capillary pressure (p_c) and disjoining pressure (Π).

In the initial stage of film thinning, p_c governs the drainage rate of a TLF, which can be calculated using,

$$p_c = \frac{2\gamma}{r_2} \tag{45}$$

where γ is surface tension of water and r_2 is bubble radius.

However, surface forces and disjoining pressure (Π) between air/water interfaces start to have major effect on the thinning rate when the thickness of TLF becomes about 200 nm. One can use extended DLVO theory [38] to determine Π,

$$\Pi = \Pi_{el} + \Pi_{vw} + \Pi_{hp} = 64 C_{el} R' T \tanh^2\left(\frac{e\psi_s}{4k'T}\right)\exp(-\kappa H) - \frac{A_{232}}{6\pi H^3} - \frac{K_{232}}{6\pi H^3} \tag{46}$$

where Π_{el} is the disjoining pressure due to electrostatic force, Π_{vw} is the disjoining pressure due to the van der Waals dispersion force, Π_{hp} is the disjoining pressure due to hydrophobic force, C_{el} is the electrolyte concentration, R' the gas constant, T the absolute temperature, e the electronic charge (1.6×10^{-19} C), ψ_s the surface potential at the air/water interfaces, k' the Boltzmann's constant, κ the reciprocal of Debye length, A_{232} the Hamaker constant between two bubbles in a medium, and K_{232} the hydrophobic constant.

When H reaches the critical rupture thickness (H_{cr}), TLF ruptures and hence bubble coalesces. Vrij et al. derived a predictive model for H_{cr} based on capillary wave theory [39-41],

$$144\gamma\left\{3H_m^{-4}\left(\left.\frac{\partial\Pi}{\partial H}\right|_{H=H_m}\right)^{-2}-2H_{cr}^{-3}\left(\left.\frac{\partial\Pi}{\partial H}\right|_{H=H_m}\right)^{-3}\left.\frac{\partial^2\Pi}{\partial H^2}\right|_{H=H_m}\right\}-\frac{3H_m^{-3}R_{film}^2}{2\left(p_c-\Pi\right)}=0 \qquad (47)$$

where $H_{cr}=0.845H_m$ and H_m is the median thickness of a TLF. The H_{cr} model shown above is a first principle model, which was further improved by Park and Yoon [36] to take the disjoining pressure contributed by hydrophobic force (Π_{hp}) into consideration. Eq. (47) can predict the critical rupture thickness (H_{cr}) in different solutions. The H_{cr} values predicted from the model can be used to predict the PB area (A_{cr}) using Eq. (42), which in turn is used to predict the bubble coarsening or the ratio ($d_{2,t}/d_{2,b}$) of bubbles between the top and bottom of a foam using Eq. (40).

Since the presence of particles in the froth will cause the local curvatures to change, in turn p_c will change from that of free films ($2\gamma/r_2$). The presence of particles will also change disjoining pressure (Π) and hence the driving force (p). The detailed calculation of new driving force p due to the presence of particles can be found in the Park's dissertation [36].

According to Reynolds' Equation, one can use numeric methods to generate the plot showing the relationship between film thickness (H) and drainage time (t_d). Since the H_{cr} is an output from the critical rupture thickness model, one can determine critical rupture time, $t_{cr,}$ by checking the H vs t_d plot. Then the bubble size ratio can be calculated using the following equation [36],

$$\frac{d_{2,b}}{d_{2,t}}=\sqrt{\exp\left(-\frac{2\ln 2}{3}\frac{h_f}{V_g t_{cr}}N_{rupture}\right)} \qquad (48)$$

where h_f is froth height, V_g is superficial gas rate, t_{cr} is critical rupture time and $N_{rupture}$ is a fitting parameter, which represents the number of films that rupture on one bubble. In the simulation, $N_{rupture}$ ranges from 1 to 12 because each bubble is assumed to have dodecahedron structure (12 faces).

Figure 2.4 shows the effect of particle hydrophobicity on the froth stability. When the particle contact angle is below 70°, the bubble size ratio becomes smaller with the increase of particle hydrophobicity, which means that the froth stability increases with the particle hydrophobicity. However, the further increase of the particle hydrophobicity will catastrophically destroy the froth. As shown, the 85° contact angle has the largest bubble size ratio in this figure, which represents the froth is the most unstable among all these cases.

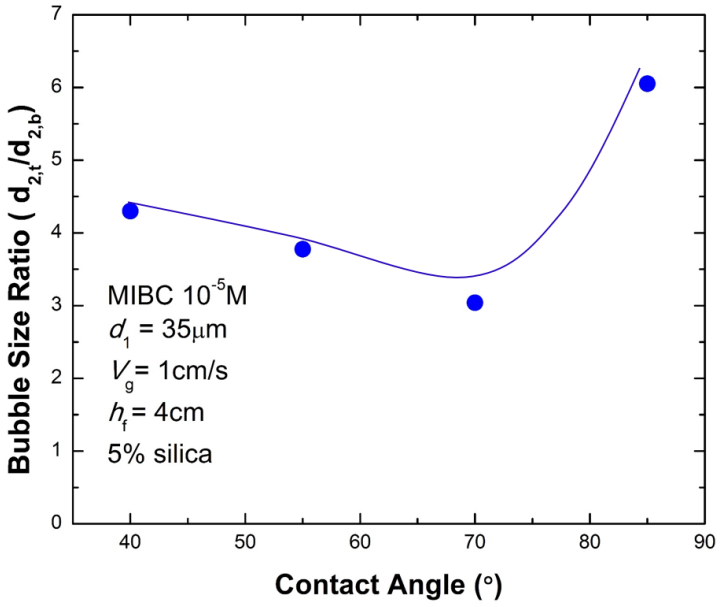

Figure 2.4: The effect of particle hydrophobicity on the bubble size ratio ($d_{2,f}/d_{2,b}$). Park, S., *Modeling Bubble Coarsening in Froth Phase from First Principles*. 2015, Virginia Tech. Used under fair use, 2015.

Figure 2.5 shows the effect of particle size on the froth stability. As shown, bubble size ratio increases significantly when the particle size becomes coarser from 11μm to 71μm, which represents the stability of the froth decreases with the increment of particle size. Both simulation and experiment results may demonstrate that fine particles have a better effect on stabilizing the froth than coarse particles [42].

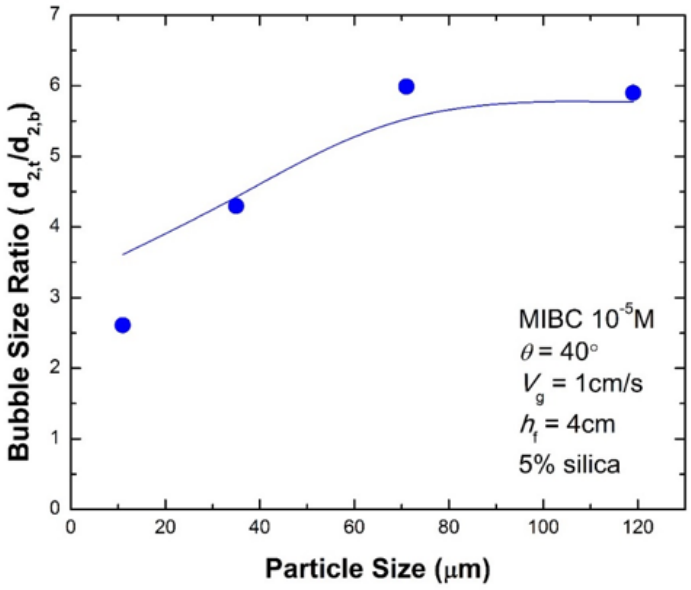

Figure 2.5: The effect of particle size on the bubble size ratio ($d_{2,t}/d_{2,b}$). Park, S., *Modeling Bubble Coarsening in Froth Phase from First Principles*. 2015, Virginia Tech. Used under fair use, 2015.

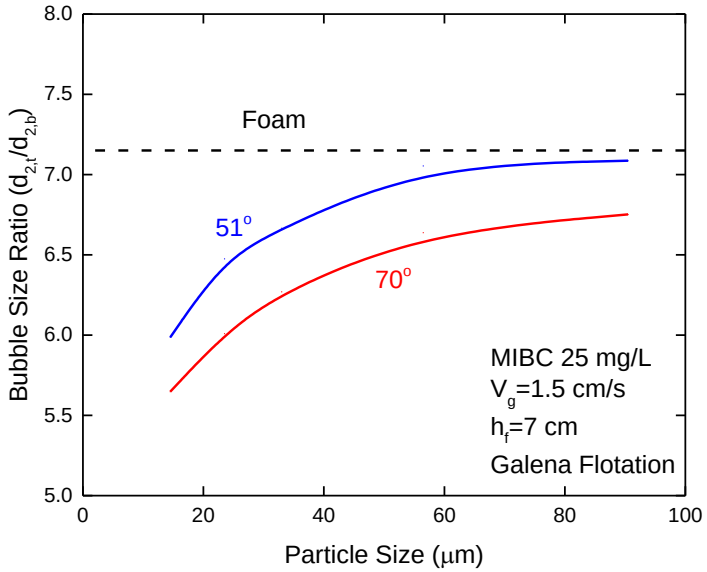

Figure 2.6: The simulation results of the bubble size ratio ($d_{2,t}/d_{2,b}$) generated from the galena flotation tests conducted by Welsby, S.D.D., *On the interpretation of floatability using the bubble load.* 2009. Used under fair use, 2015.

Figure 2.6 shows the simulation results of the bubble size ratio ($d_{2,t}/d_{2,b}$) generated from the galena flotation tests conducted by Welsby *et. al*. The operating parameters can be found in the original thesis [6]. In this case, the adjustable parameter $N_{rupture}$ is 8. As shown, the bubble size ratio in the foam is larger than that in the froth. Increasing in particle size will lead to an increase in bubble size ratio, which proves that the fine particle has better effects on stabilizing the froth than the coarse particles. Furthermore, as one increase the contact angle from 51^o to 70^o, at a given particle size, there is a reduction in bubble size ratio in Figure 2.6, which means increasing contact angle of particles in the froth may benefit the stability of froth when contact angle is below 70^o.

2.3 Behavior of Composite Particles

2.3.1 Predicting contact angles

An empirical liberation model has been developed to evaluate the contact angle of mineral particles from mineral surface liberation data. At present, weighted geometric mean equation has been applied. The equation below shows the method to calculate the contact angle for composite particles,

$$\bar{\theta} = \left(\prod_{i=1}^{n} \theta_i^{a_i b_i} \right)^{1/\sum_{i=1}^{n} a_i} = \exp\left(\frac{\sum_{i=1}^{n} a_i b_i \ln \theta_i}{\sum_{i=1}^{n} a_i} \right) \tag{49}$$

where n is the number of types of the minerals in the composite, θ_i is the contact angle of the mineral i, a_i is the fractional surface liberation of the mineral i, b_i is the fitting parameter to change the weight for the mineral i and $\bar{\theta}$ is the contact angle for a composite particle. For a 2-componet particle, the Eq. (49) can be simplified as below:

$$\bar{\theta} = \exp\left(a_1 b_1 \ln \theta_1 + a_2 b_2 \ln \theta_2 \right) \tag{50}$$

Below is an example to show the contact angle calculation of a 2-component particle. The particle surface is composed of 60% galena and 40% silica (gangue), *e.g.*, Figure 2.7.

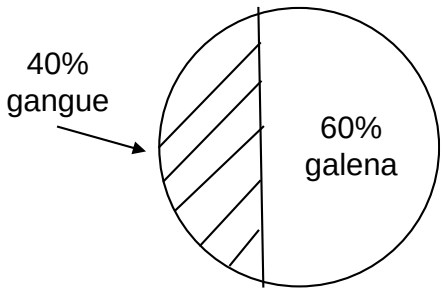

Figure 2.7: An example of contact angle calculation for a composite particle.

Assuming that the contact angle for galena and silica are 70º and 5º, respectively, and two fitting parameters both equal to 1, one can calculate the contact angle for the composite particle as follows:

$$\bar{\theta} = \left(\prod_{i=1}^{n} \theta_i^{a_i b_i} \right)^{1/\sum_{i=1}^{n} a_i} = \exp\left(\frac{\sum_{i=1}^{n} a_i b_i \ln \theta_i}{\sum_{i=1}^{n} a_i} \right)$$

$$= \exp\left(\frac{0.6 \times 1 \times \ln 70 + 0.4 \times 1 \times \ln 5}{0.6 + 0.4} \right)$$

$$= 24.36^{o}$$

Therefore, the average contact angle for this composite particle is 24.36º.

Chapter 3: MODEL VALIDATION

3.1 Pilot-scale Flotation Test

The pilot-scale galena flotation tests were conducted by Welsby et. al. [43] to show the effects of particle size and surface liberation on the size-by-class flotation recovery (R_{ij}) and galena flotation rate constants (k_{ij}), where subscript *i* represents different size classes and subscript *j* represents different liberation classes. While specific details of the whole experiments can be found in the original thesis [6], the relevant test parameters related with the simulation process are listed in Table 3.1. Size analysis and liberation analysis were conducted on the feed samples using cyclosizing and Mineral Liberation Analyzer (MLA), respectively. The size-by-class mass distribution matrix of feed is shown in Table 3.2. The contact angles for galena and gangue are assumed to be 70^o and 5^o, respectively. The fitting parameters for corrected contact angle of composite particles are $b_1 = 0.957$ and $b_2 = 1.973$. The adjustable parameter in the bubble coarsening model *C* equals to 22.71 in the simulation.

Table 3.1 Pilot-scale flotation test parameters. Welsby, S., S. Vianna, and J.-P. Franzidis, *Assigning physical significance to floatability components.* International Journal of Mineral Processing, 2010. **97**(1): p. 59-67. Used under fair use, 2015.

Variable	Value
Frother Type	MIBC
Frother Dosage (mg/kg)	25
Residence Time (min)	4.68
Froth Height (cm)	7
Impeller Speed (rpm)	1200
Air Flow Rate (L/min)	110
Cell Volume (L)	40
Cell Area (cm^2)	35x35
Solids in the slurry (wt.%)	44.31
Pulp Density (g/mL)	1.48

Table 3.2: Size-by-class mineral liberation data (m_{ij}) for pilot-scale galena flotation simulation.

m_{ij} (%)	Liberation Classes (%)												
Particle Size Classes (µm)	**0**	**0~10**	**10~20**	**20~30**	**30~40**	**40~50**	**50~60**	**60~70**	**70~80**	**80~90**	**90~100**	**100**	**Total Mass**
+106	22.46	4.12	0.64	0.27	0.15	0.05	0.03	0.02	0.01	0.01	0.01	0.05	27.83
+75/-106	9.28	1.05	0.17	0.08	0.06	0.04	0.03	0.01	0.01	0.02	0.03	0.16	10.95
+38/-75	15.02	1.73	0.31	0.16	0.11	0.08	0.06	0.05	0.04	0.05	0.13	0.96	18.70
+28/-38	4.70	0.30	0.07	0.04	0.03	0.02	0.02	0.02	0.01	0.02	0.05	1.57	6.85
+19/-28	7.15	0.30	0.07	0.04	0.03	0.02	0.02	0.02	0.01	0.01	0.05	1.44	9.15
+10/-19	8.87	0.27	0.09	0.05	0.03	0.04	0.03	0.02	0.02	0.02	0.07	2.05	11.55
-10	11.09	0.14	0.11	0.06	0.04	0.04	0.03	0.04	0.03	0.04	0.05	3.29	14.96
Total	78.57	7.90	1.46	0.69	0.45	0.29	0.22	0.17	0.15	0.16	0.40	9.51	100.00

(A)

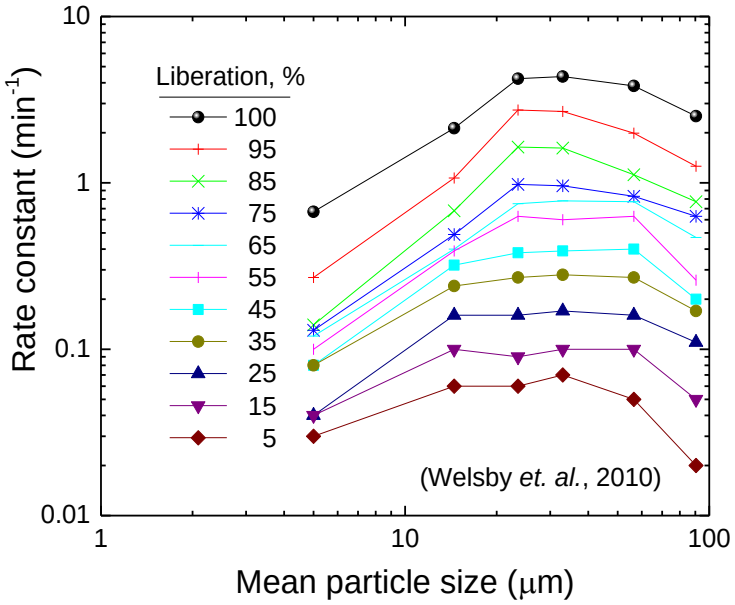

(B)

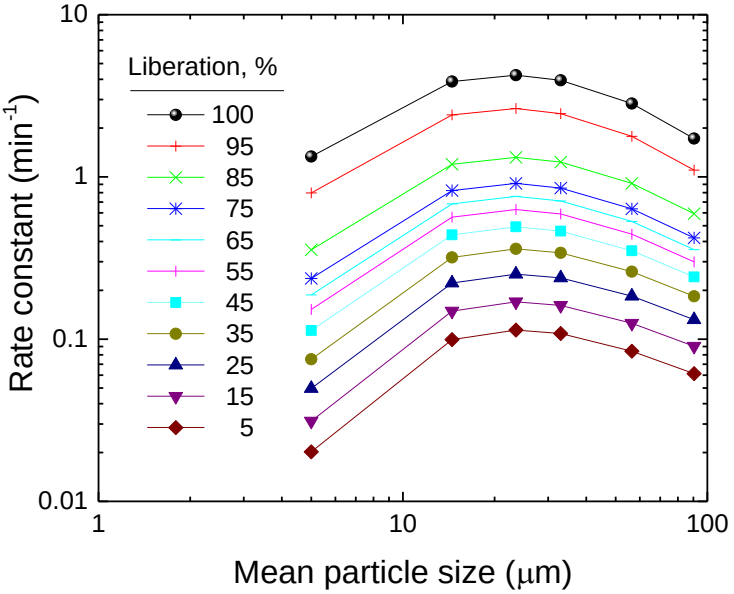

Figure 3.1: Comparison of size-by-class overall rate constants (k_{ij}) between experiment results (A) and simulation results (B). The experimental data was obtained from Welsby, S.D.D., *On the interpretation of floatability using the bubble load.* 2009. Used under fair use, 2015.

(A)

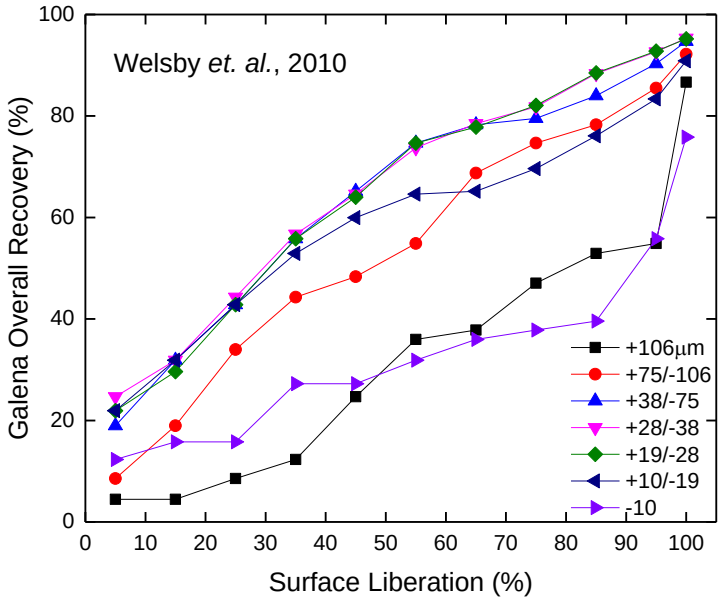

(B)

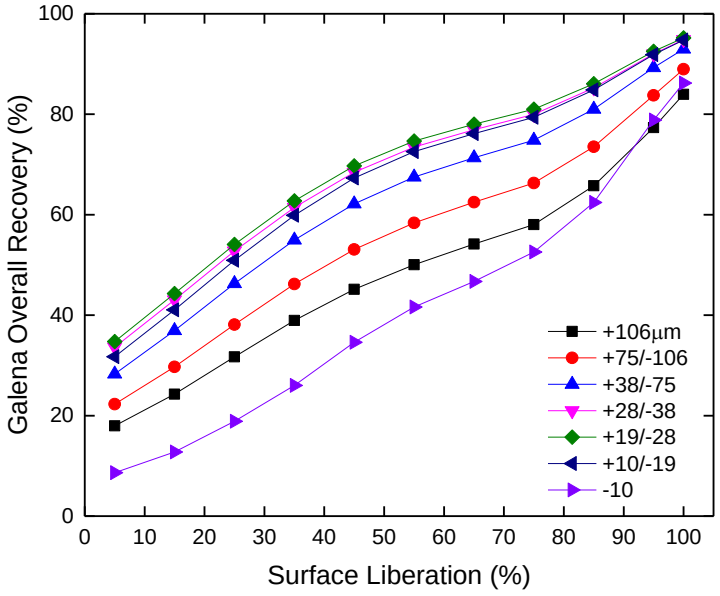

Figure 3.2: Comparison of size-by-liberation overall flotation recovery (R_{ij}) between experiment results (A) and simulation results (B). The experimental data was obtained from Welsby, S.D.D., *On the interpretation of floatability using the bubble load.* 2009. Used under fair use, 2015.

3.1.1 Size-by-liberation Simulation Results

Figure 3.1 (A) shows the effect of particle size and surface liberation on the overall rate constant (k_{ij}), which is generated from the flotation experiments. Figure 3.1 (B) is the simulation results from the flotation model. As shown, with the mean particle size increasing, at a given liberation class, the flotation rate constants first increase, then reach the highest value, and finally decrease. For particles at a given size class, the higher the surface liberation class, the bigger the overall flotation rate constant. Furthermore, when the particles are fully-liberated, the rate constant reaches the maximum at each specific particle size.

Figure 3.2 shows the effect of particle size and surface liberation on the galena recovery (R_{ij}). One can convert rate constants into recoveries for a continuous flotation cell under perfectly mixed condition by using the Eq. (34). Figure 3.2 (A) is generated from flotation tests, while Figure 3.2 (B) is the output from the flotation model. It can be seen that at a given particle size the overall galena recovery increases with increasing the degree of surface liberation for all particle sizes. The fully-liberated particles have the highest recoveries among other particles at a given particle size. The optimum particle size range for galena flotation locates between 20 μm and 40 μm, since the curves which represent +28/-38 and +19/-28 size classes are higher than any other curve in the figure. The model prediction is excellent for medium-size particles. For coarse and fine particles, however, the difference between the test results and model results is large. For some reason, the model overestimates the recovery of coarse and fine particles.

3.1.2 Size-by-size Simulation Results

By combining the information of size-by-liberation feed (m_{ij}) and recoveries (R_{ij}), one can get the size-by-size overall flotation recoveries (R) and size-by-size overall rate constants (k) for galena particles, which is shown in Figure 3.3. Figure 3.3 (A) shows the experiment results while Figure 3.3 (B) shows the simulation results. The simulation of k and R is quite similar with the results from the experiments. As shown, fine particles and coarse particles have relatively small k and R. There is one peak in each curves, which represents that the medium-size particles have the highest k and R values. In this case, one can see that the optimum particle size interval for galena flotation is also 20 to 40 μm, which is consistent with the conclusion drawn from Figure 3.1.

(A)

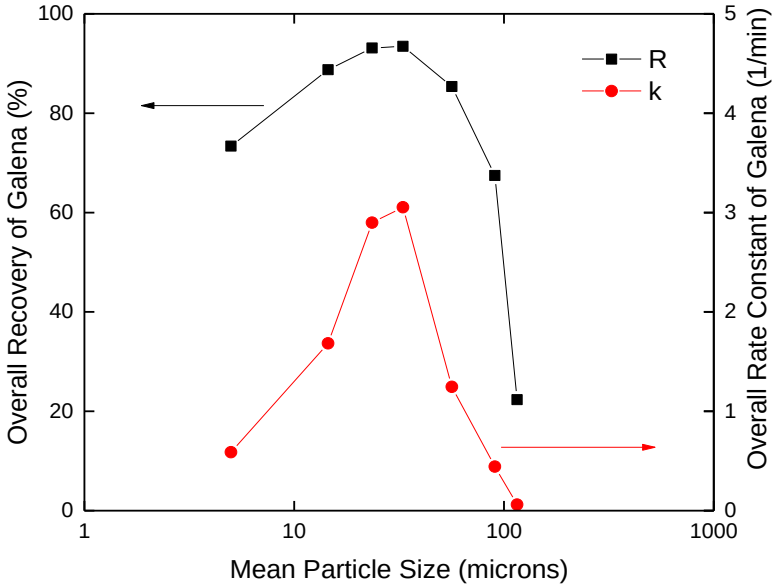

(B)

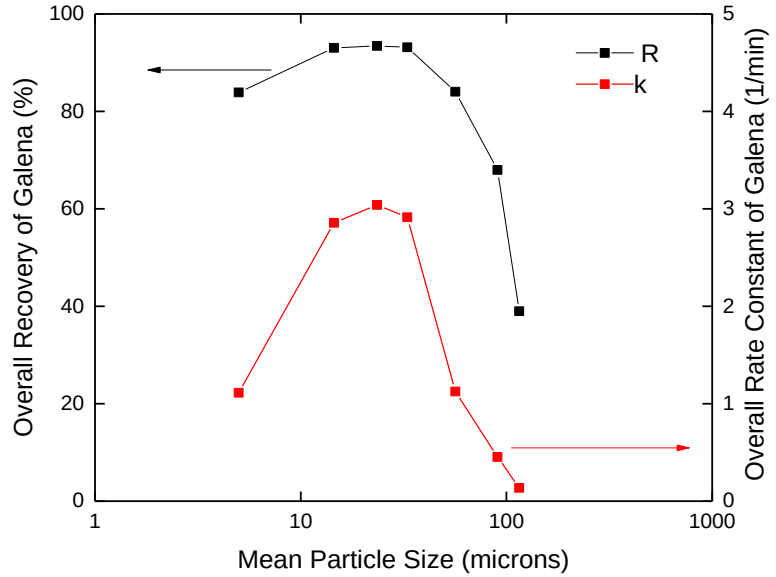

Figure 3.3: Comparison of size-by-size overall flotation recovery (*R*) and overall rate constants (*k*) between experiment results (A) and simulation results (B). The original data was from Welsby, S., S. Vianna, and J.-P. Franzidis, *Assigning physical significance to floatability components.* International Journal of Mineral Processing, 2010. **97**(1): p. 59-67. Used under fair use, 2015.

(A)

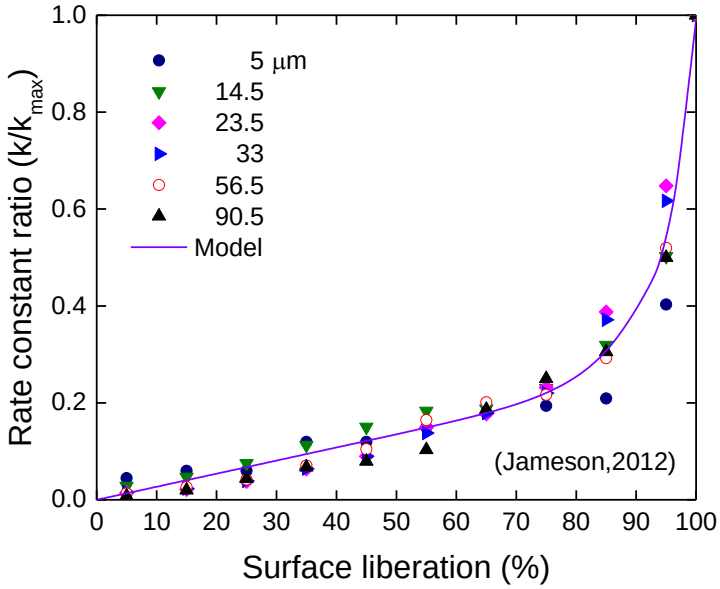

(B)

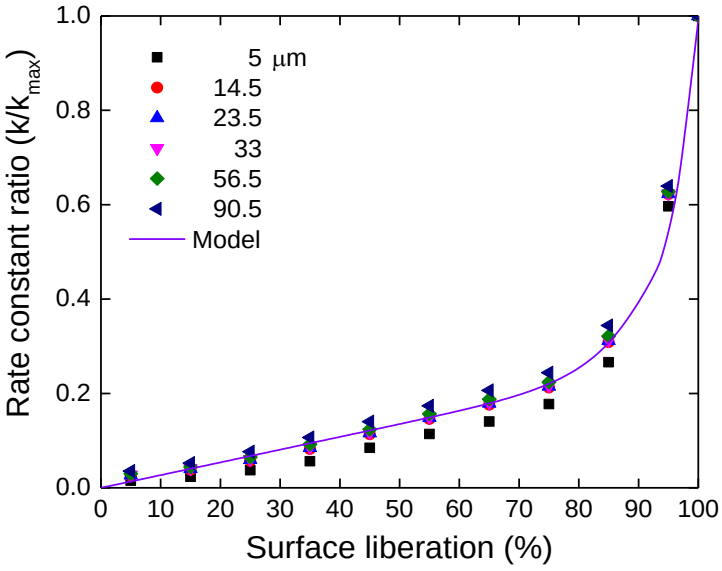

Figure 3.4: Comparison of rate constant ratio k/k_{max} (normalized k) between experiment results (A) and simulation results (B). Figure (A) was from Jameson, G.J., *The effect of surface liberation and particle size on flotation rate constants.* Minerals Engineering, 2012. **36**: p. 132-137. Used under fair use, 2015.

3.1.3 Normalized Rate Constants Simulation

The normalized flotation rate constant, k/k_{max}, which is also called rate constant ratio, is defined as the ratio of the rate constant at a given particle size and liberation class, to the rate constant for the full-liberated particles of the same size. Figure 3.4 (A) shows the relationship between rate constant ratio (k/k_{max}) and the surface liberation class. It can be seen that the rate constant ratio as a function of surface liberation is essentially the same for each particle size. An pure empirical equation, therefore, was developed by Graeme J. Jameson [44] to fit the different points in Figure 3.4 (A), which is represented by the solid curve in Figure 3.4 (A). Below is the equation,

$$L = axe^{bx^c} \tag{51}$$

where $L=k/k_{max}$ and x is the fractional liberation ($0 \le x \le 1$); the constants have the values $a=0.27$, $b=1.30$ and $c=10.80$.

The results shown in Figure 3.4 (A) is extremely important because it shows that the rate constant for a fully-liberated ore only depends on the hydrodynamics and surface chemistry. The rate constant of a particle of a given liberation class can be first determined by that of the fully-liberated particle of the same size. Then a factor, k/k_{max}, can be applied, which represents the effect of liberation.

Figure 3.4 (B) is the k/k_{max} simulation results from the floatation model. The solid curve in this graph is the same as the curve in Figure 3.4 (A), in order to compare the simulation results with the experiment results conveniently. At a given surface liberation, the simulated data points locate closer with each other compared to the data points from experiments, especially for the higher liberated particles. However, the overall simulation results seem to be similar with the experiment results.

The Jameson's equation, however, has some flaws. Firstly, the equation includes three fitting parameters, a, b and c, which makes the model complex. Secondly, as the mineral is fully-liberated, the rate constant ratio from the equation is not exact 1, which is not consistent with the definition of the rate constant ratio. A new empirical equation, therefore, has been developed by using statistical analysis, which is shown below,

$$L = \frac{x}{a - bx^6} \tag{52}$$

where $a=4$ and $b=3$. In the new equation, only two fitting parameters are used. As shown in Figure 3.5, one can easily see that two curves based on Eqs. (51) and (52) respectively are extremely similar, and almost overlap with each other. It is obvious that the new equation, which is simple, has the same function on predicting rate constant ratio from surface liberation data as the Jameson's equation [44].

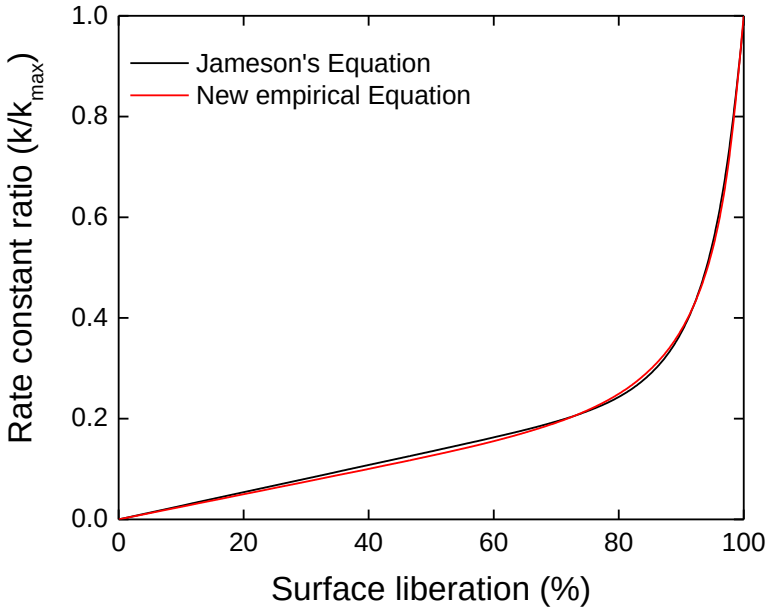

Figure 3.5: Comparison between Jameson's equation and Eq. (52) (new empirical equation) shows that both equations have almost the same function on predicting k/k_{max} as a function of surface liberation.

Eqs. (51) and (52) are significant findings, although both are empirical. With these two equations, one may predict flotation performances by testing only single-size but different-liberation ore samples, which is much simpler than testing all-size fractions. The detailed procedure of model prediction is shown below:

Firstly, one can separate a single-size sample from the flotation feed, *e.g.*, +28/-38, and use QEM-scan or MLA technology to determine the surface liberation. Next, one can do flotation tests using all-size sample as the feed, then analyze test results, and finally calculate the flotation recoveries and rate constants for the particles that have different surface liberations in +28/-38 size class. At this time, one can use flotation model to simulate the k_{ij} for different liberated particles by adjusting fitting parameters in the flotation model, *e.g.*, b_1, b_2 and C. Meanwhile, since rate constants have been determined, the k/k_{max} can be simulated by applying Eq. (52). In Figure 3.6, one can clearly see that the results from the model and the results from the experiments are very similar, which can be demonstrated by the fact that the curve based on Eq. (52) goes through almost every experimental points. At present, one can predict the k/k_{max} of different-liberation but the same-size particles. As discussed before, it is reasonable to assume that k/k_{max} is only dependent on the surface liberation of particles and independent of particle size. Since the rate constants of fully-liberated particles can be simulated from the flotation model, one may calculate the rate constants (k_{ij}) for any particles by multiplying k/k_{max} at given liberation class with the rate constant for the fully-liberated particles of the same particle size.

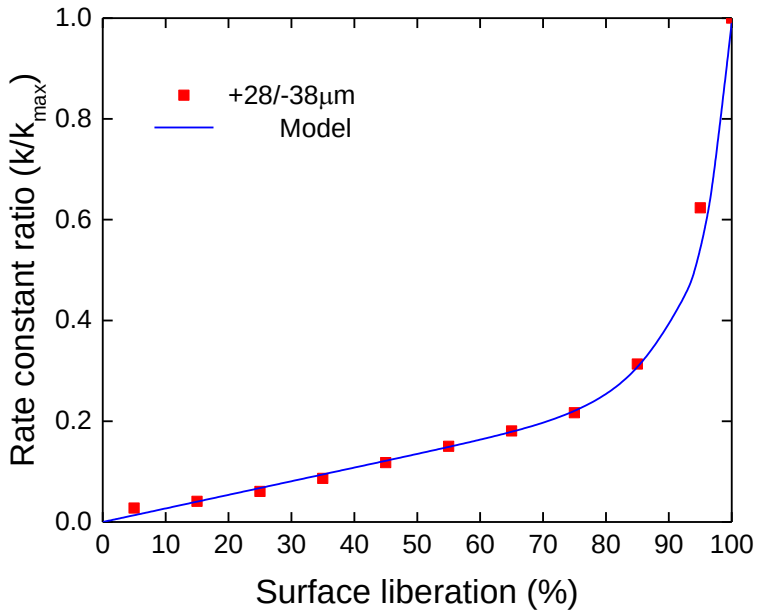

Figure 3.6: Comparison between k/k_{max} from single-size class particles (+28/-38 μm) and k/k_{max} from the model.

Table 3.3 shows the procedure of flotation model prediction directly. The green data in the table are the results from flotation tests. The red ones are the simulated data from flotation model, which are rate constants for fully-liberated particles that have various sizes. The blue data represents the k_{ij} calculated by multiplying the red values with the respective k/k_{max} for different-size particles. Figure 3.7 shows the comparison between the simulation from single-size fraction feed and the simulation from all-size fraction feed. The solid curve represents the Eq. (52), which is the same in both figures. Because only single-size fraction is used in the simulation, the points in Figure 3.7 (A) locates much closer to the solid curve compared to the points in Figure 3.7 (B). However, generally, the difference between these two figures is small, which makes it doable to use single-size fraction to predict the flotation performance. This is a new method to simulate flotation process, which is quite efficient and economical. Great amounts of time and cost can be saved since only single-size class particles will be studied in surface liberation analysis. Meanwhile, the accuracy and the preciseness of the new simulation procedure can be compared with those from old simulation process.

Table 3.3: Size-by-class rate constant (k_{ij}) simulation results based on single size fraction feed. Data in green is flotation test results, data in red is generated from flotation model and data in blue is calculated by multiplying the red data with k/k_{max} at a given surface liberation and a given particle size.

k_{ij} (min^{-1})	Liberation Classes (%)										
Particle Size Classes (µm)	**0~10**	**10~20**	**20~30**	**30~40**	**40~50**	**50~60**	**60~70**	**70~80**	**80~90**	**90~100**	**100**
+106	0.02	0.05	0.08	0.11	0.14	0.17	0.20	0.24	0.32	0.61	1.12
-106+75	0.02	0.07	0.12	0.16	0.21	0.26	0.31	0.37	0.49	0.93	1.72
-75+38	0.04	0.11	0.19	0.27	0.34	0.42	0.50	0.61	0.81	1.53	2.83
-38+28	0.07	0.11	0.17	0.28	0.39	0.60	0.78	0.96	1.62	2.69	4.36
-28+19	0.06	0.17	0.29	0.40	0.52	0.63	0.75	0.91	1.22	2.30	4.24
-19+10	0.05	0.16	0.26	0.37	0.47	0.58	0.69	0.83	1.11	2.10	3.88
-10	0.02	0.05	0.09	0.13	0.16	0.20	0.24	0.29	0.38	0.73	1.34

(A)

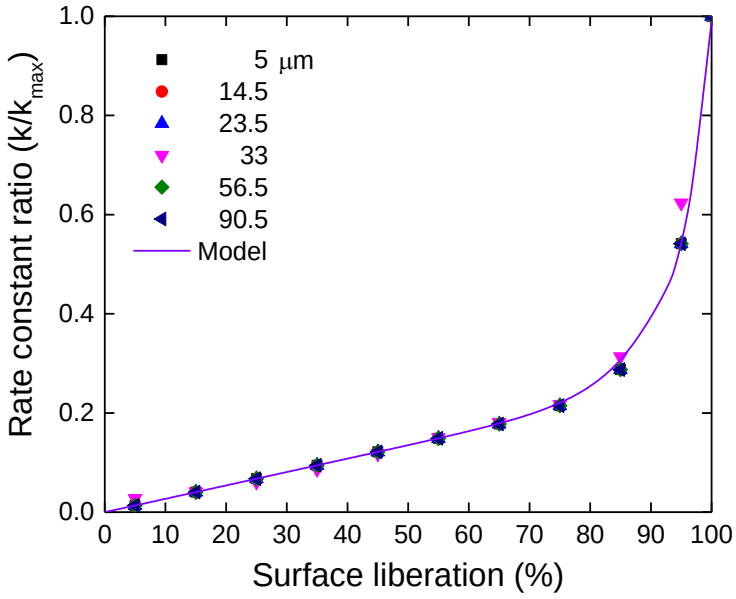

(B)

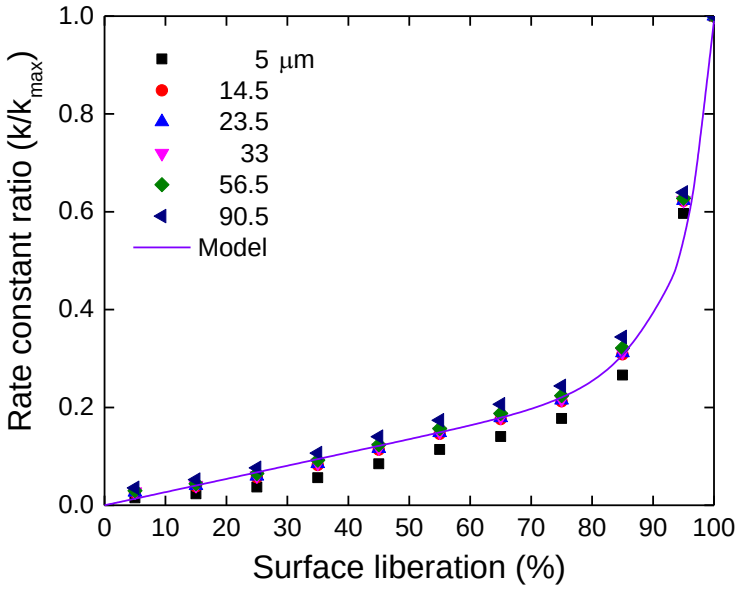

Figure 3.7: Comparison between the predictions of rate constant ratio k/k_{max} from single-size class (A) and k/k_{max} from all-size classes (B).

3.2 Laboratory-scale Flotation Test

A batch flotation experiment data was provided by Outotec to show the relationship between particle size and recovery of the chalcopyrite, pyrite and other minerals (gangue). The ore sample in the flotation test was porphyry. About 70,000 particles in the feed sample were analyzed by QEM*SEM technology, which could give us the information of particle surface liberation. Based on the original sizing and surface liberation data, one can generate a size-by-liberation feed matrix, *e.g.*, Table 3.4, which shows the mass distribution of the feed sample in each size class and liberation class. There are six size classes and six liberation classes in Table 3.4. In the flotation model, the size-by-liberation mass distribution table of feed is an elementary input. The accuracy and precision of the feed matrix significantly affect the simulation results from the flotation model.

Table 3.4: Size-by-liberation mass distribution (m_{ij}) of porphyry sample in batch flotation test.

m_{ij} (%)	Surface Liberation Classes (%)						
Particle Size Classes (μm)	**0~20**	**20~40**	**40~60**	**60~80**	**80-100**	**100**	**Total Mass**
+150	18.36	0.06	0.00	0.00	0.02	0.03	18.48
+106/-150	15.54	0.25	0.03	0.03	0.11	0.03	15.98
+75/-106	11.69	0.10	0.01	0.02	0.03	0.11	11.97
+38/-75	15.02	0.17	0.05	0.06	0.07	0.38	15.75
+20/-38	9.14	0.03	0.02	0.05	0.02	0.25	9.51
-20	28.24	0.01	0.01	0.00	0.00	0.07	28.32
Total	97.98	0.61	0.12	0.17	0.26	0.87	100

Table 3.5: Assumed value for input parameters in chalcopyrite flotation simulation.

Variable	Value
Bubble ζ-potential (V)	-0.03
Particle ζ-potential (V)	-0.05
Contact angle for gangue (^{o})	5
Contact angle for chalcopyrite (^{o})	70
Fitting parameter b_1	1
Fitting parameter b_2	1.5

The porphyry flotation test was conducted in a 4-liter flotation cell. The weight of sample was 1.5 kg. The frother used in the test was Dow 250, which was a common-used frother in industry. The dosage of Dow 250 was 60 g/ton. The specific energy in the cell was 3.33 kW/m^3. The solid weight content in the pulp was 34%. The height of froth was 5 mm. The flotation time was 16 min. The superficial gas rate in the test was 0.28 cm/s.

Although there are several test parameters which are provided by Outotec, the input data for simulation is still not enough. Table 3.5 lists a series of assumed values for parameters used in the simulation, *e.g.*, contact angle, bubble ζ-potential, and particle ζ-potential.

3.2.1 Flotation Test Results

Figure 3.8 shows the size-by-size flotation recoveries of chalcopyrite, pyrite and other minerals (gangue). As shown, the recoveries of chalcopyrite and pyrite are both much higher than the recovery of gangue, from which one can conclude that the flotation is an effective separation way to remove gangue from valuable minerals. For the fine particles, the selectivity of flotation is not as good as that of coarse particles. One possible reason is that in the froth phase large amount of fine particles can come into the concentrate by entrainment, during which hydrophobic minerals cannot be distinguished from hydrophilic gangue. For coarse particles, the recovery of chalcopyrite decreases faster than the recovery of pyrite.

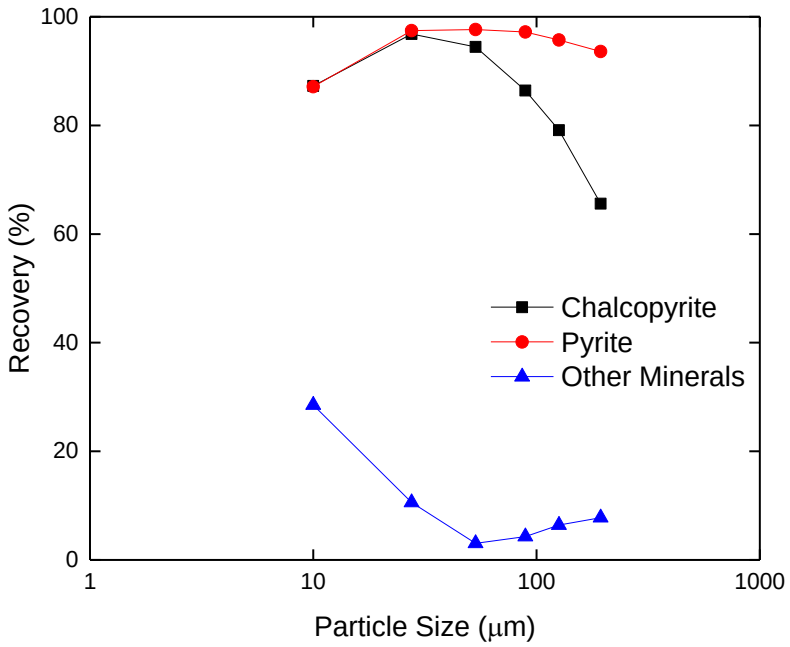

Figure 3.8: Size-by-size recovery (R) of chalcopyrite, pyrite and other minerals from the laboratory-scale flotation tests.

By applying the Eq. (34), one can convert the recoveries of different minerals into the overall rate constants of different minerals, which is shown in Figure 3.9. One can see that the rate constants of gangue are almost 0 at different particle sizes, while the rate constants for chalcopyrite and pyrite are much larger than 0 and reach the highest value when the particle size is between 20 μm and 60 μm.

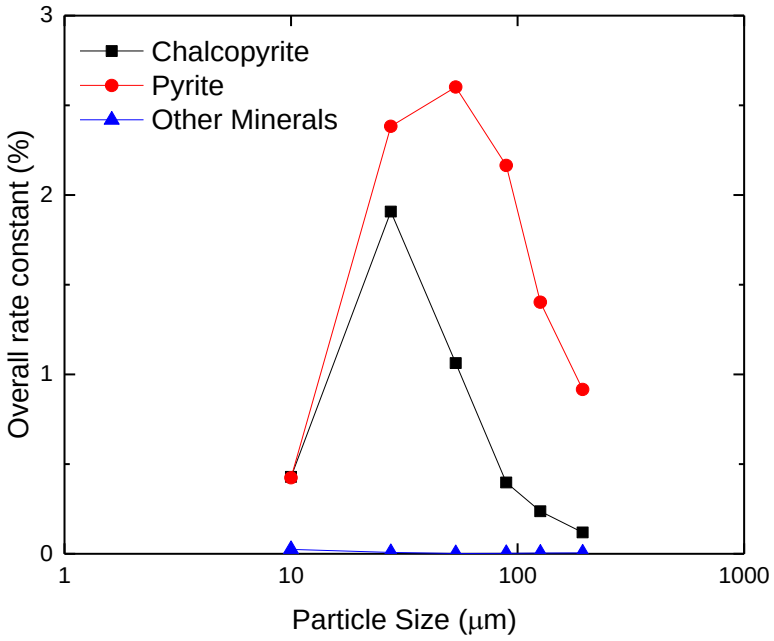

Figure 3.9: Size-by-size overall rate constants (k) of chalcopyrite, pyrite and other minerals converted from the overall flotation recovery (R).

3.2.2 Size-by-liberation Simulation Results

After putting all necessary parameters into the simulator, one can simulate size-by-liberation flotation results. The simulated data is shown in Table 3.6. Figure 3.10 presents the simulation results of overall rate constants (k_{ij}). At a given particle size, the higher liberated mineral particles have the larger rate constants. At a given surface liberation, the rate constant is as function of particle size. There is always a peak on each curve when the particle size is around 30 μm, which represents the optimum particle size for the flotation.

Figure 3.11 shows the overall chalcopyrite recovery simulation results obtained by varying particle sizes and particle surface components. The results suggests that the recovery for the particle of which diameter is smaller than 100 μm is extremely high. For the large particles that are larger than 100 μm, the recovery substantially decreases with the increasing particle size, regardless of the particle surface liberation. A proper explanation for this phenomenon is that the probability of detachment (P_d) is much larger for coarse particles than that of fine particles, which will cause that coarse particles detach from bubble surfaces more frequently. Large

probability of detachment for coarse particles may overwhelm the effect of surface liberation on recovery. Thus, the particles that have a high surface liberation are always having high flotation recovery when the particle size is less than 100 μm. However, when the particle size is larger than 100 μm, a higher surface liberation of particles does not essentially mean a higher flotation recovery of these particles.

Table 3.6: Size-by-liberation simulated rate constants (k_{ij}) of chalcopyrite in the batch flotation test.

k_{ij} (%)	Surface Liberation Classes (%)					
Particle Size Classes (μm)	**0~20**	**20~40**	**40~60**	**60~80**	**80-100**	**100**
+150	0.03	0.02	0.02	0.01	0.01	0.01
+106/-150	0.16	0.19	0.24	0.28	0.41	0.40
+75/-106	0.25	0.37	0.56	0.80	1.23	1.33
+38/-75	0.31	0.51	0.87	1.40	2.25	2.55
+20/-38	0.32	0.56	0.99	1.66	2.69	3.10
-20	0.22	0.39	0.70	1.16	1.82	2.08

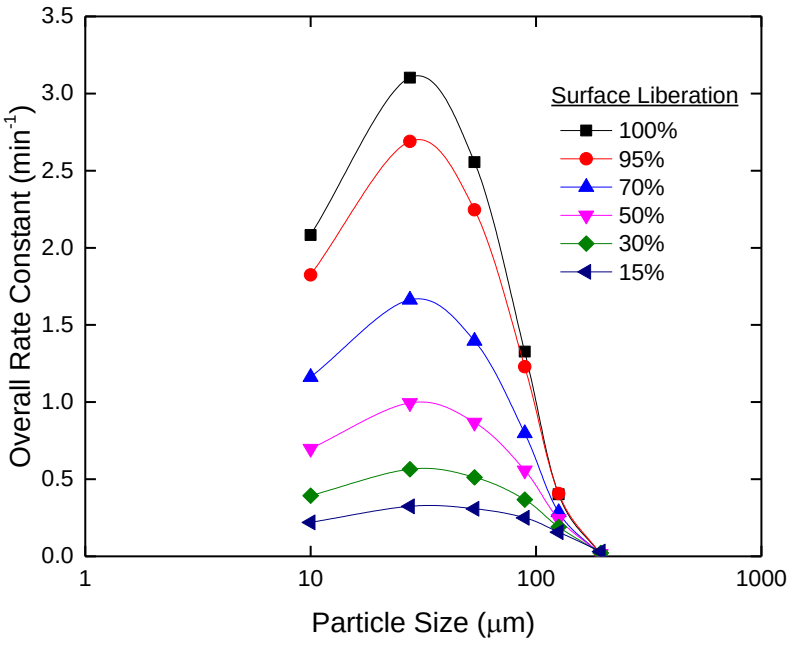

Figure 3.10: Size-by-liberation overall rate constants (k_{ij}) of chalcopyrite from flotation model.

The conclusions drawn from Figure 3.10 and Figure 3.11 are consistent with the conclusions from the pilot-scale flotation simulation, which can be great evidences to support the rightness of the flotation model.

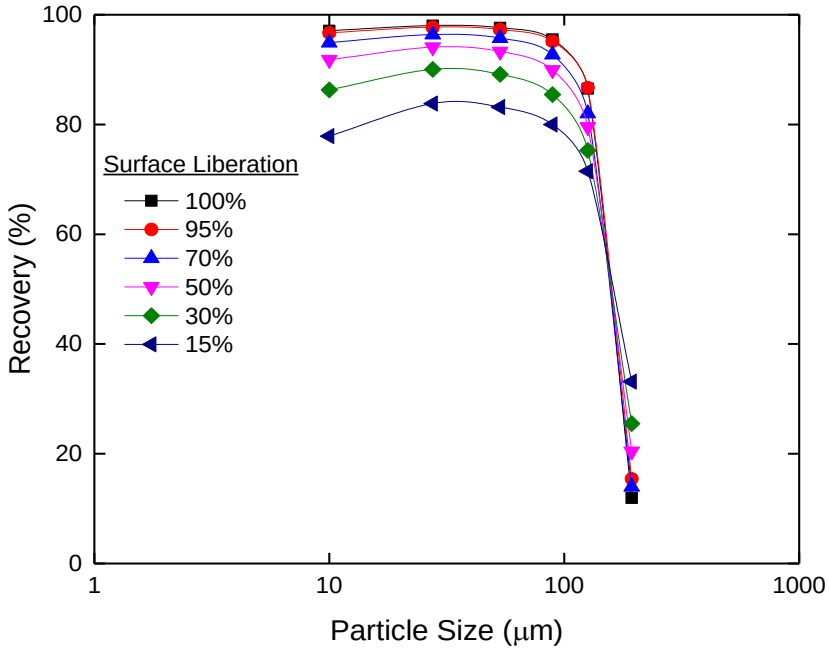

Figure 3.11: Size-by-liberation overall flotation recovery (R_{ij}) of chalcopyrite from flotation model.

3.2.3 Size-by-size Simulation Results

Since the size-by-liberation data of rate constant and recovery has been simulated, one can further simulate size-by-size recoveries and rate constants of the flotation. Figure 3.12 compares the simulation results with the results from flotation tests. In two plots, the red dots represent the data obtained from tests and the black solid curves represent the simulation results from the model. It is shown in Figure 3.12 (A) that the overall recovery of chalcopyrite first increases to a maximum value and then decreases rapidly with the increase of the particle size. Figure 3.12 (B) shows the same trend of overall rate constant as a function of particle size. There are some gaps between the experimental points and simulation curves in both figures, however, the general pattern of the simulated curves fits the experiment results well, that is to say, the flotation model is quite reliable, which can make reasonable predictions after entering a series of necessary input parameters.

(A)

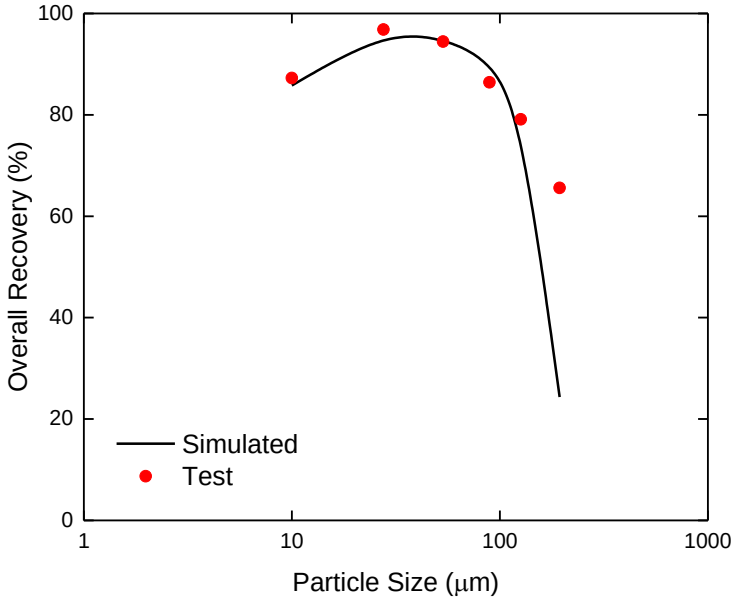

(B)

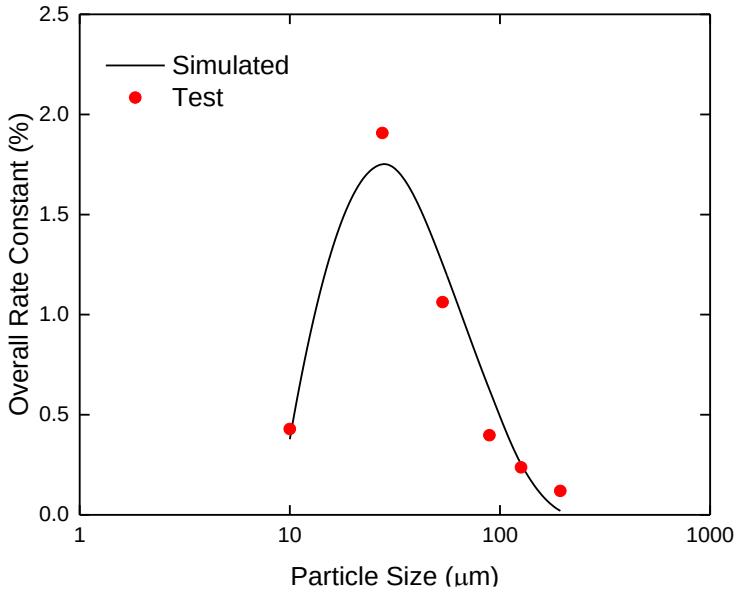

Figure 3.12: Experiment results (red dots) and simulation results (black curves) of size-by-size overall recovery (A) and overall rate constants (B).

3.2.4 Normalized Rate Constant Analysis

Since the size-by-liberation rate constants have already been determined, one can study the rate constant ratio (k/k_{max}) by applying the same method as before. As shown in Figure 3.13, at a given surface liberation, the rate constant ratios for different-size particles are very similar, which is represented by the points aggregating with each other in the vertical direction. The solid line in the figure represents the model for rate constant ratio, which is Eq. (52). In this specific case, $a=1.30$ and $b=0.30$. The model fits the test data well, which makes it possible to predict the flotation performance from single-size but different-liberation particles.

However, it is necessary to note here that Figure 3.13 only includes four different size classes, in which the mean particle sizes are all less than 100 μm. It seems that the rate constant ratio for coarse particles does not subject to this property, which is that the flotation rate constant only depends on particle surface liberation, but has nothing to do with the particle size. For coarse particles, the effect of particle size on the rate constant ratio may be so strong that one cannot simply ignore it. This finding is quite similar with Jameson's, who excluded the particles that were larger than 106 μm when analyzing the rate constant ratio.

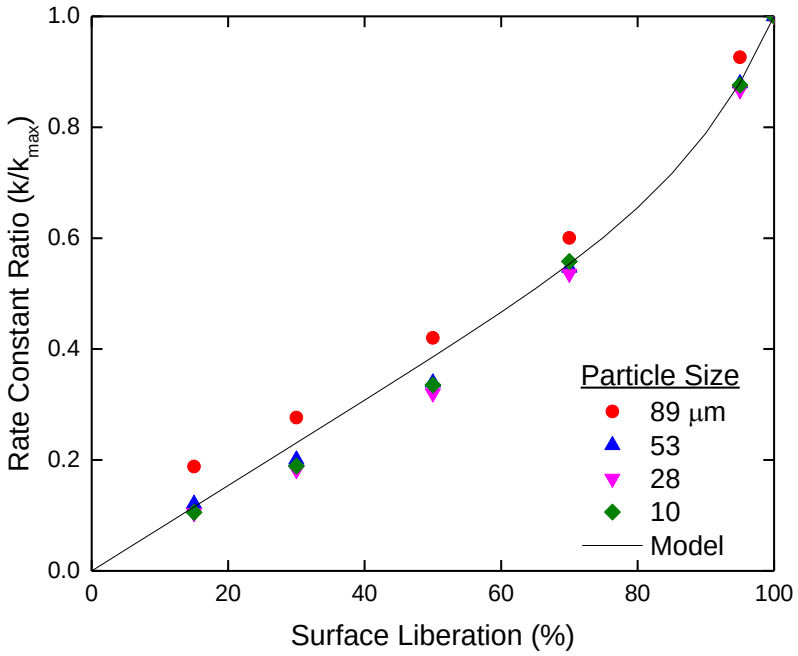

Figure 3.13: Simulation of normalized rate constant (k/k_{max}) as functions of surface liberation and particle size.

Figure 3.14 (A) and (B) show the simulation results of size-by-class rate constants from all-size fractions feed and those from single-size fraction feed, respectively. The overall patterns of these two figures are extremely similar. However, one main difference between these two figures is that the rate constants for coarse particles (>100 μm). The rate constants from all-size

fractions are larger than those from single-size fraction when the particle size is large than 100 μm.

(A)

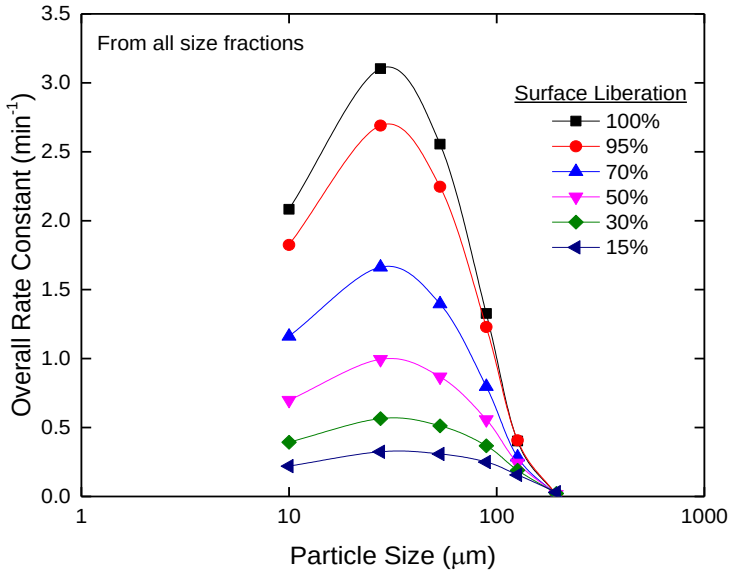

(B)

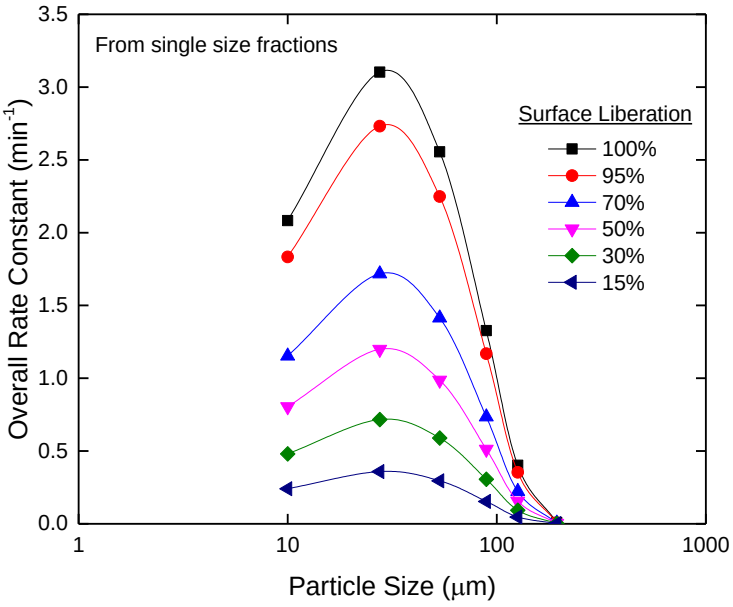

Figure 3.14: Comparison between size-by-class rate constants (k_{ij}) simulated from all-size fractions feed and those simulated from single-size fraction feed.

In sum, one can conclude that for a particle which is less than 100 μm, the normalized flotation rate constant (k/k_{max}) depends only on the surface condition of the particle. For particles that are larger than 100 μm, however, one may still need to concede that particle size has strong effect on the normalized rate constant (k/k_{max}). Therefore, in the present work, it is only applicable to predict flotation performance from single-size fraction feed when the particle size is smaller than 100 μm.

Chapter 4: SIMULATION

The flotation model discussed and validated in previous chapters is developed from first principles, which considers both surface chemistry parameters and hydrodynamic parameters that have effects on flotation process. Therefore, the model can predict the flotation recovery, rate constant and product grade from both physical and chemical conditions. In the present work, several factors that affect flotation performance have been studied, *e.g.*, particle size, surface liberation (contact angle), ζ-potential, energy input, *etc.*

4.1 Single Cell Flotation

Effects of different parameters are studied, such as particle size, surface liberation, superficial gas rate and ζ-potential. The flotation feed information is the same as Table 3.2, which is a size-by-class galena mass distribution matrix.

4.1.1 Surface Liberation (Contact Angle)

Figure 4.1 shows the effect of surface liberation and particle size on the overall rate constants of a galena flotation. As the surface liberation of galena increases, the contact angle (θ)

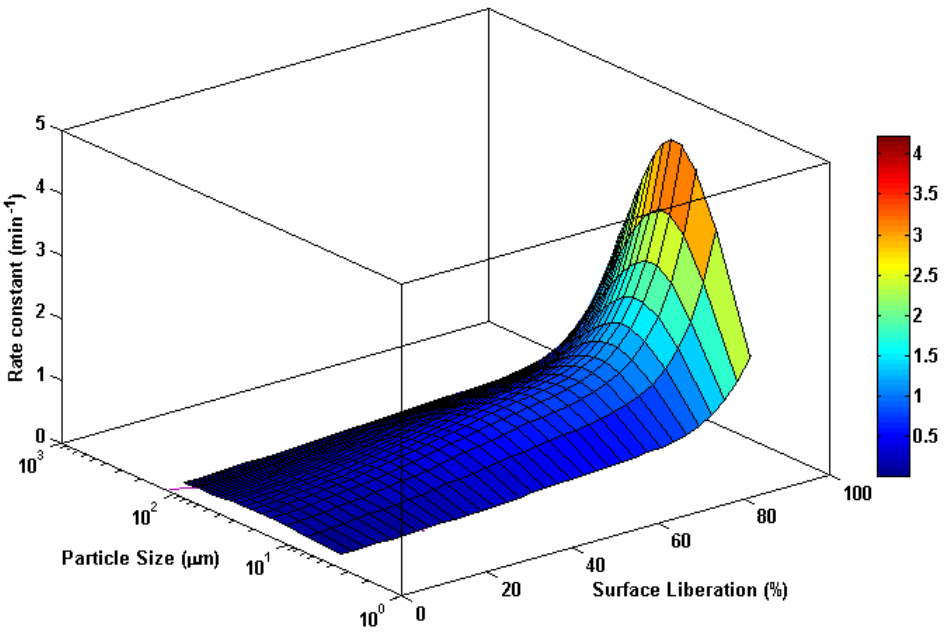

Figure 4.1: Effect of particle size and surface liberation on flotation rate constants (k). Input parameters: aeration rate, 1.5 cm/s; energy dissipation rate, 15 kW/m^3; frother, 25 mg/L MIBC; residence time, 4.68 min; froth height, 7 cm; particle ζ-potential, -80 mV.

for the composite particles increases. As shown, at a given particle size, a higher liberated particle has a higher flotation rate constant, which proves that increasing particle hydrophobicity benefits the rate of flotation. The fully liberated particles, which have the larger contact angle than any other particles have, have the largest flotation rate constant in each size class.

Figure 4.2 shows a contour plot for the changes in recovery as functions of particle size and particle surface liberation. At a given particle size, the flotation recovery increases with increasing the surface area of galena. It is shown that there is a valley on the plot, which represents the optimum particle size for the maximum flotation recovery. In this typical case, the optimum particle size for the flotation is between 20 μm and 30 μm.

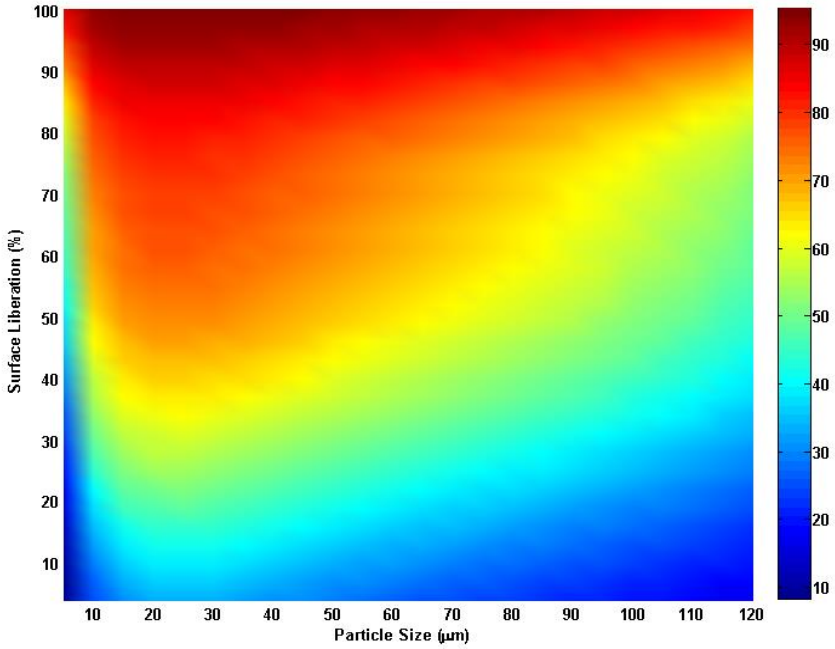

Figure 4.2: Effect of particle size and surface liberation on flotation recovery (R). Input parameters: aeration rate, 1.5 cm/s; energy dissipation rate, 15 kW/m^3; frother, 25 mg/L MIBC; residence time, 4.68 min; froth height, 7 cm; particle ζ-potential, -80 mV.

Eqs. (20) and (21) show that the hydrophobic force constant for bubble-particle interaction (K_{132}) increases with the increasing particle contact angle (θ) or with increasing particle surface liberation. Hydrophobic force plays an important role in decreasing the energy barrier (E_1), which causes the increase of probability of bubble-particle attachment (P_a) and hence the flotation rate constant (k) and overall recovery (R).

4.1.2 Froth Height

Figure 4.3 shows a contour plot for the changes in recovery as functions of froth height and particle size. As shown, there is a remarkable reduction for the recovery of coarse particles when the froth height increases. A high froth height means a high probability of particle detaching from bubble in the froth phase, which would cause a decrease in froth recovery (R_f), hence the overall recovery decrease. Generally, the froth height has more significant effects on the recovery of coarse particles than on that of fine particles.

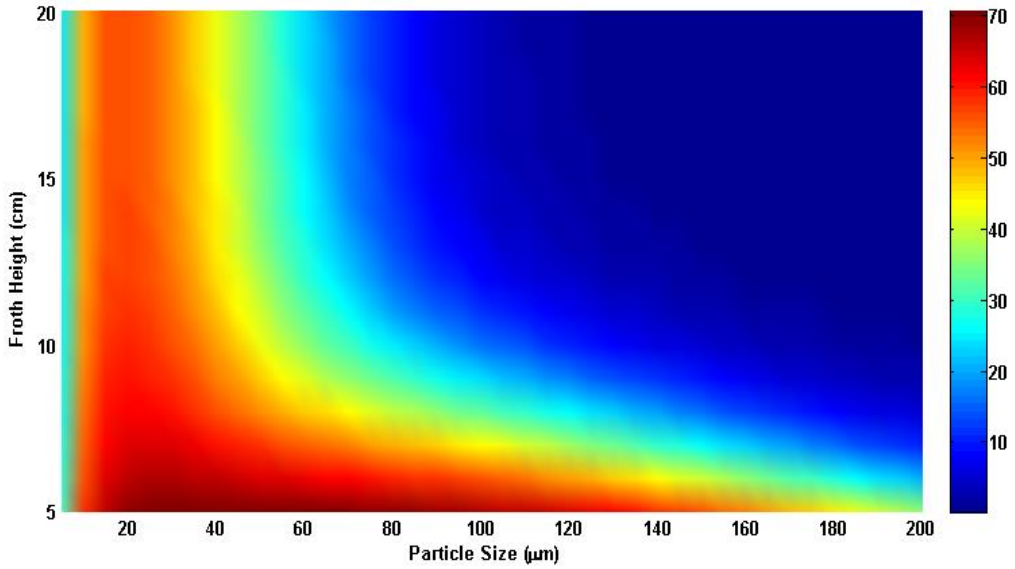

Figure 4.3: Effect of particle size and froth height on flotation recovery (R). Input parameters: aeration rate, 1.5 cm/s; energy dissipation rate, 15 kW/m^3; frother, 25 mg/L MIBC; residence time, 4.68 min; particle ζ-potential, -80 mV; θ = 35^o.

4.1.3 Superficial Gas Rate

Figure 4.4 shows a contour plot for recovery varied with particle size and superficial gas rate (or aeration rate). At a given particle size, a rise in airflow rate leads to an increase of flotation recovery. This can be explained by that increasing superficial gas rate decreases particle residence time in the froth phase (τ_f), hence the particles have less probability to detach from bubble surface in the froth phase. This finding is in agreement with many industrial column flotation results by other researchers in the past [45].

4.1.4 Energy Dissipation Rate

Figure 4.5 is a surface plot showing the effects of changing the mean energy dissipation rate (ε) on overall flotation rate constant (k). The simulation results are plotted versus particle

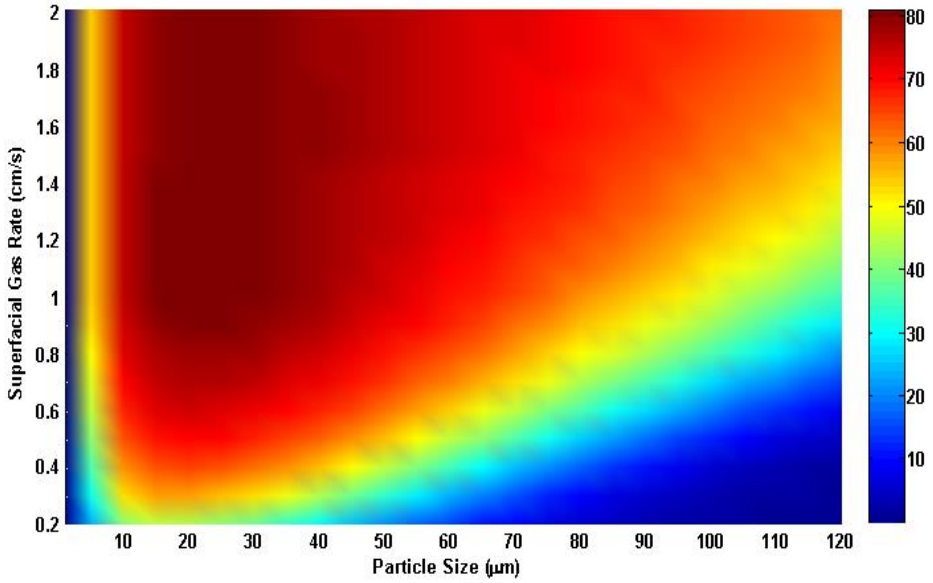

Figure 4.4: Effect of particle size and superficial gas rate on flotation recovery (*R*). Input parameters: energy dissipation rate, 15 kW/m^3; frother, 25 mg/L MIBC; residence time, 4.68 min; froth height, 7 cm; particle ζ-potential, -80 mV; θ = 45^o.

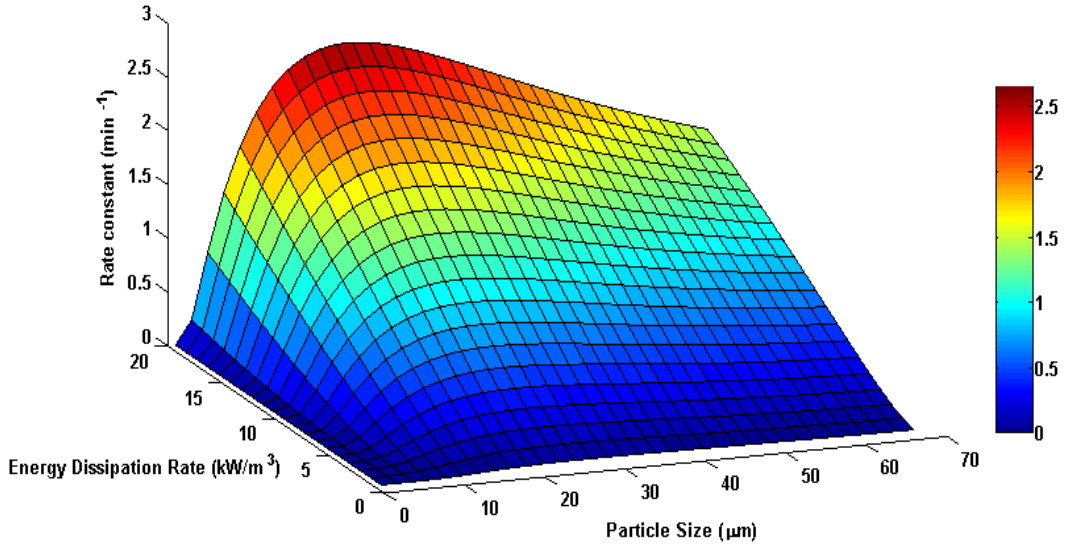

Figure 4.5: Effect of particle size and energy dissipation rate on overall rate constant (*k*). Input parameters: aeration rate, 1.5 cm/s; frother, 25 mg/L MIBC; residence time, 4.68 min; froth height, 7 cm; particle ζ-potential, -80 mV; θ = 60^o.

size (d_1). Generally, at a given particle size, increasing ε can result in the increase of flotation rate constant, which can be attributed to the increase in the kinetic energy for bubble-particle attachment. This finding is in agreement with the work done by Ahmed and Jameson [46], who showed that high agitation rate led to an increase in the overall flotation rate constant. Another reason for this phenomenon is that the bubble size (d_2) decreases with increasing ε, according to the bubble generation model [22]. Therefore, micro-bubbles have been applied in the flotation process in order to increase recovery for fine mineral particles.

4.1.5 ζ- Potential

Figure 4.6 shows flotation recovery as functions of particle size and particle ζ-potential. It is generally acknowledged that in sulfide minerals flotation the ζ-potential of bubbles and particles are both negative. It is shown in the plot that a decrease in particle ζ-potential has a good effect on the fine particle recovery, which is due to a reduction of electrostatic energy (V_E) and hence a decrease in energy barrier (E_1) for bubble-particle attachment. This finding is consistent with the former work of many investigators, who concluded that the flotation recovery reached the highest value when the magnitude of ζ-potential reached minimum [47-49]. For the coarse particles, however, it seems that the effect of particle ζ-potential on recovery is quite small. The reason is probably that for large particles, the beneficial effects of low particle ζ-potential can be overcome by the large probability of detachment (P_d).

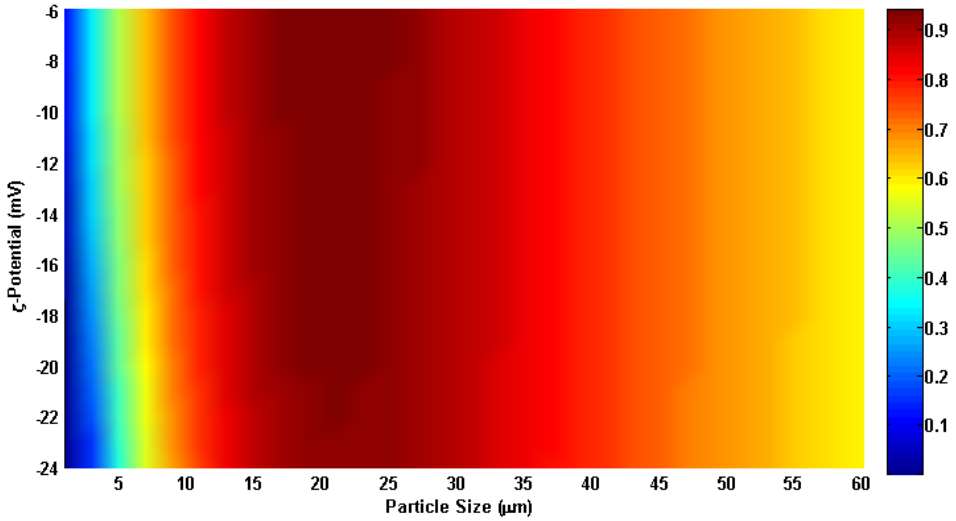

Figure 4.6: Effect of particle size and ζ-potential on overall rate constant (k). Input parameters: aeration rate, 1.5 cm/s; energy dissipation rate, 15 kW/m^3; frother, 25 mg/L MIBC; residence time, 4.68 min; froth height, 7 cm; $\theta = 45^o$.

4.2 Flotation Circuit

In this section, two simulations of chalcopyrite flotation circuits were conducted, in which the effect of a re-grinding unit and the effect of different collectors (contact angles) have been studied. Table 4.1 shows part of the input parameters used for simulation. The flotation feed input is a size-by-class chalcopyrite mass distribution matrix (Table 4.2).

Table 4.1: Input parameters for flotation circuit simulation.

Variable	Value
Cell Volume (m^3)	42.48
Column Volume (m^3)	172
Contact Angle (gaugue)	5^o
Contact Angle (chalcopyrite)	55^o & 80^o
Gangue Specific Gravity	2.65
Chalcopyrite Specific Gravity	4.19
Particle ζ-potential (mV)	-8
Bubble ζ-potential (mV)	-30

Table 4.2: Size-by-class mineral liberation data (m_{ij}) for chalcopyrite flotation circuit simulation. Soni, G., *Development and Validation of a Simulator based on a First-Principle Flotation Model*. 2013, Virginia Tech. Used under fair use, 2015.

m_{ij} (%)	Surface Liberation Classes (%)				
Particle Size Classes (μm)	**0~30**	**30~60**	**60~90**	**90~100**	**Total Mass**
+150/-425	10.52	0.08	0.05	0.13	10.78
+106/-150	17.19	0.17	0.11	0.45	17.92
+75/-106	11.82	0.12	0.08	0.48	12.50
+53/-75	10.53	0.06	0.05	0.61	11.25
+38/-53	8.94	0.06	0.03	0.55	9.58
+32/-38	6.31	0.02	0.01	0.47	6.82
+24/-32	6.67	0.02	0.02	0.53	7.24
+17/-24	9.05	0.03	0.01	0.60	9.70
+12/-17	8.56	0.02	0.01	0.55	9.15
+8.6/-12	4.76	0.01	0.01	0.28	5.06
Total	94.37	0.60	0.37	4.66	100.00

Circuit arrangement:

Figure 4.7 shows the original circuits used in Escondida chalcopyrite flotation plant in Antofagasta, Chile. The circuit in the red block is simulated by the flotation model. The feed of the simulated circuits is cyclone overflow, which directs to a bank of forty flotation cells served as the rougher flotation circuit. The rougher concentrates are re-grinded by the grinding mill, which is operated in closed circuit with a cluster of cyclone classifiers. The cyclone underflow is returned to the ball mill, while the overflow proceeds to a cleaner circuit using flotation columns. The cleaner tails are scavenged by a bank of twenty cells. The cleaner-scavenger concentrates are combined with the feed for the cleaner circuit.

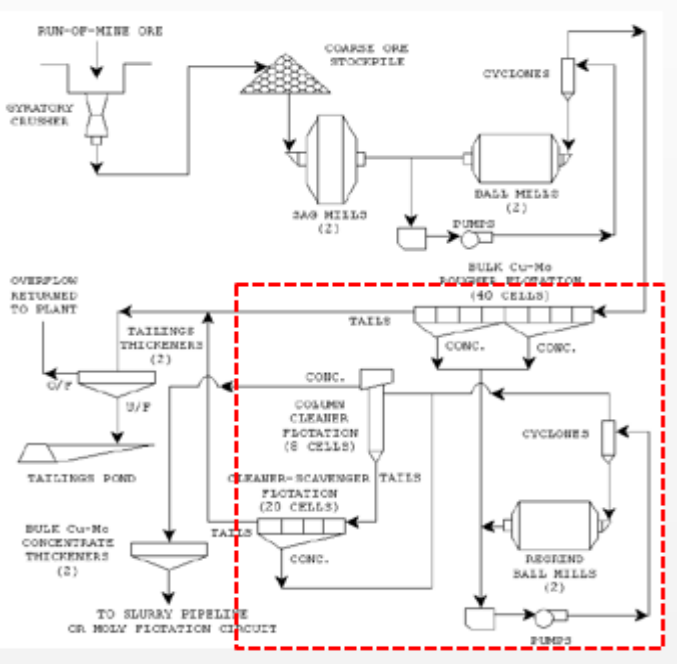

Figure 4.7: Flotation circuit used at Escondida chalcopyrite flotation plant in Chile. The circuit in the red block is to be simulated by the flotation simulator.

Two circuits arrangement are considered for the simulation purpose, which are both shown in Figure 4.8. Figure 4.8 (A) is a circuit with a re-grinding mill, which is similar to the circuit used in Escondida. The only difference is that there are cyclone classifiers before the re-grinding mill in Escondida flowsheet while the simulated flowsheet does not consider the effect of the cyclone classifiers. Figure 4.8 (B) is another simulated circuit, in which there is no re-grinding mill before the cleaner flotation column. Note here that the re-grinding mill is simulated using a ‘pseudo grinding model’ developed by Aaron Noble, which is based on the mass balance of materials in and out of the re-grinding mill.

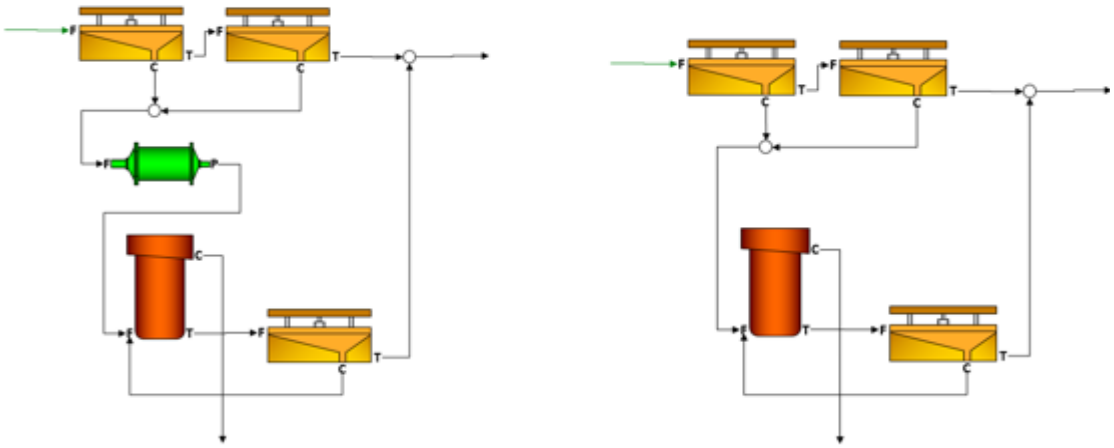

Figure 4.8: Circuits to be simulated. Circuit (A) includes a re-grinding mill, which is similar with the re-grinding circuit in Escondida flotation plant. Circuit (B) does not include a re-grinding mill.

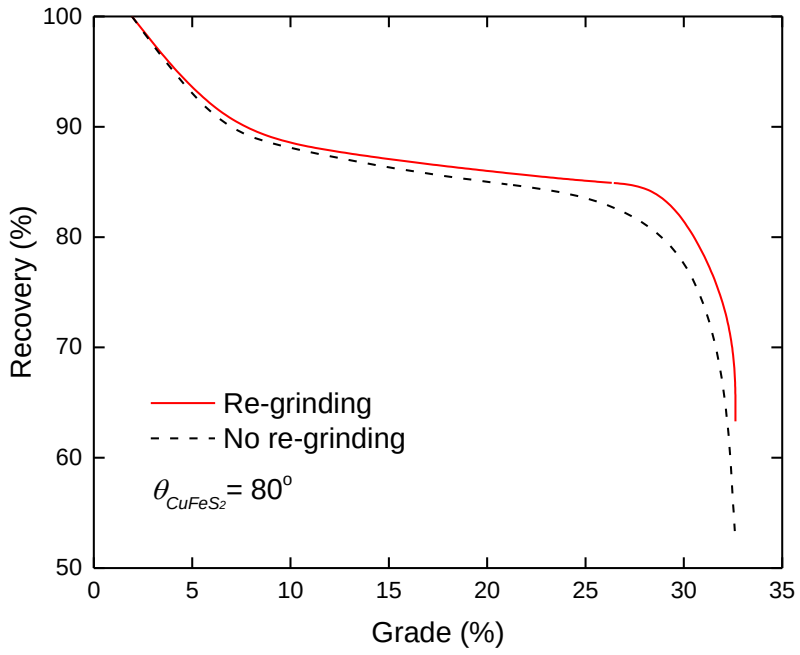

Figure 4.9: Effect of re-grinding unit on chalcopyrite grade-recovery curve.

4.2.1 Effect of Re-grinding Unit

Effect of the re-grinding unit on flotation performance is studied and the simulation results are presented in the recovery *vs.* grade plot, *e.g.*, Figure 4.9. The dashed curve represents the circuit without re-grinding unit, while the solid curve represents the circuit with re-grinding unit. The contact angle for chalcopyrite is 80^o in this simulation. It can be deduced that the re-grinding unit has a good effect on the flotation performance from Figure 4.9, since the solid curve (Re-grinding) locates a little bit higher than the dashed curve (No re-grinding). The reason is that re-grinding can better liberate the mineral particles and decrease the coarse particle percentage in the feed to cleaner flotation column.

Figure 4.10 shows the particle size analysis from the simulator at different locations in the circuit. One can see an obvious shift of median diameter, D_{50}, in the figure. The feed to rougher bank has the largest D_{50}, which is larger than 50 μm. After the rougher bank flotation, the average particle size significantly decreases since the recovery of large particles in the rougher cell is very low. The re-grinding mill will further decrease the D_{50} to around 20 μm, which is the optimum particle size range for froth flotation. Therefore, the re-grinding unit benefits the overall flotation recovery.

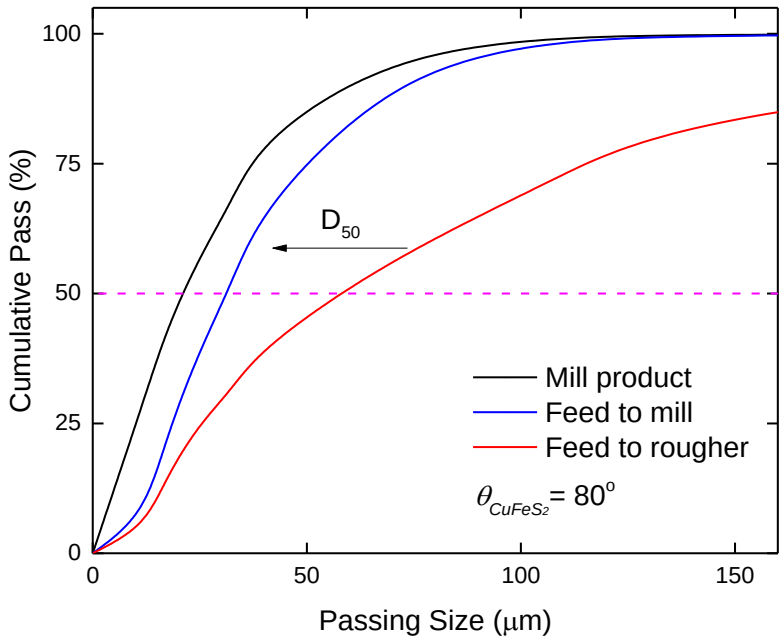

Figure 4.10: Size distribution curves of the materials at different locations in the simulated circuit.

4.2.2 Effect of Different Collectors (Contact Angle)

The effect of contact angle on flotation recovery of chalcopyrite is also studied by plotting the grade-recovery curves. Figure 4.11 shows that an increase of contact angle from 55^o to 80^o results in a slight upward shift of the recovery-grade curve, which proves that increasing contact angle can help increase the circuit performance.

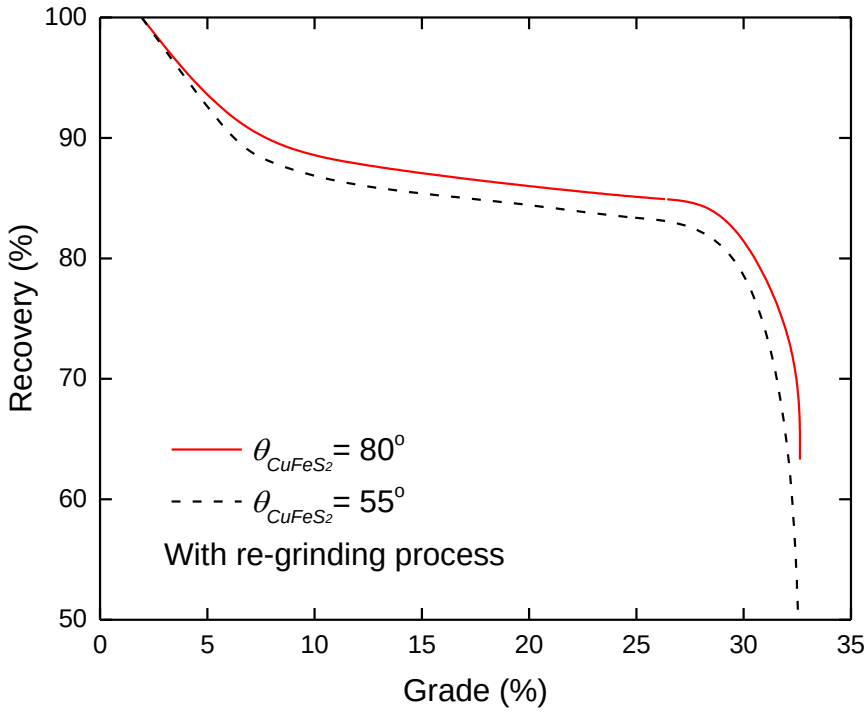

Figure 4.11: Effect of contact angle on chalcopyrite grade-recovery curve.

Figure 4.12 shows the size-by-size recovery in the rougher flotation bank. As shown, there is a significant increase in the recovery when the contact angle of chalcopyrite increases from 55^o to 80^o. The optimum particle size for chalcopyrite flotation is around 25 μm. From this figure, one can conclude that it is of great importance to use a strong collector to increase contact angle of valuable minerals in the flotation process.

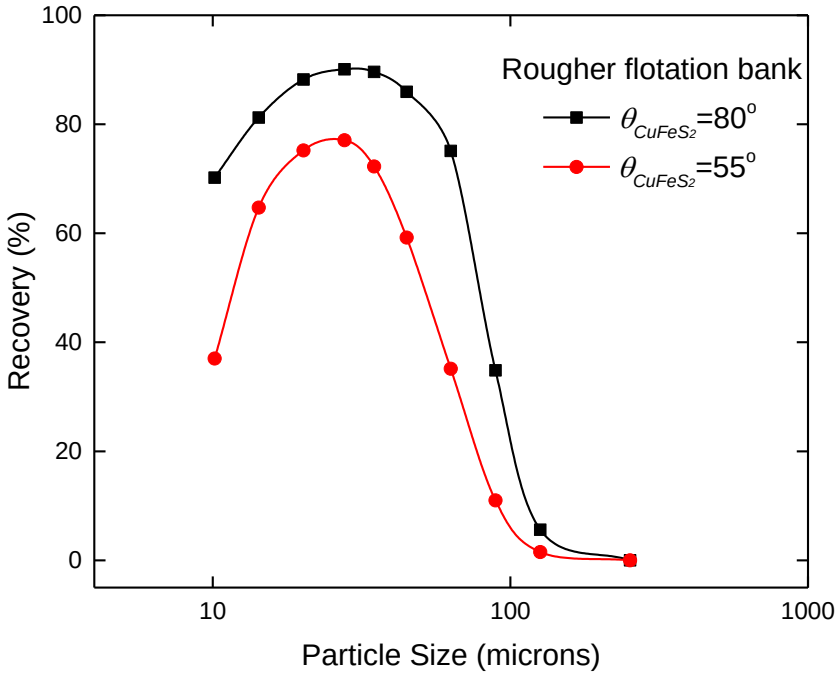

Figure 4.12: Effect of contact angle on chalcopyrite recovery in the rougher flotation bank.

Chapter 5: SUMMARY AND CONCLUSION

5.1 Conclusion

First principle flotation models can provide us better understanding of each sub-process in the flotation. The model developed at Virginia Tech, which was the first such model, can predict the performance of single flotation unit or flotation circuits without large numbers of preliminary laboratory flotation tests. The model takes both hydrodynamic and chemistry parameters in the flotation process into consideration. The primary findings and contributions presented in the thesis are summarized below.

1. In the present work, the flotation model has been verified using the flotation test results obtained by other researchers. The model predictions are in good agreement with both the laboratory-scale and pilot-scale test results, validating the first-principle flotation model developed at Virginia Tech.

2. A bubble coarsening froth model has been incorporated into the flotation model/simulator for the first time. The extended model can provide a better understanding of the effect of bubble coalescence in froth phase. However, bubble-coarsening model does not include the effects of the particle size and particle hydrophobicity yet.

3. A computer simulator has been developed for a froth model that can predict the effects of particle size and particle hydrophobicity. The model has been developed recently at Virginia Tech [36]; however, the model/simulator has not yet been incorporated into the extended flotation model developed from first principles.

4. Analysis of the size-by-class flotation rate constants reported in the literature shows that the rate constants (k_{ij}) can be normalized by the maximum flotation rate constant (k_{max}) obtained with the fully-liberated particles [44]. Thus, a series of k_{ij} *vs*. fractional surface liberation (x) plots can be reduced to a single k/k_{max} *vs*. x plot, which makes it possible to reduce the number of samples that need to be analyzed for surface liberation using a costly and time-consuming liberation analysis. It has been found in the present work that the flotation rate constants predicted from the first-principle flotation model can also be normalized by the maximum rate constants predicted for fully liberated particles.

5. The number of parameters to represent the $k/k_{\max}$ *vs*. x plots has been reduced from three to two by means of a statistical analysis.

6. A series of parameters that affect flotation recovery and rate constants are studied using the flotation simulator based on the first principle flotation model. The simulation results show that the flotation rate constant and recovery are critically dependent on particle size, surface liberation, particle hydrophobicity (contact angle), froth height, superficial gas rate, energy dissipation rate, and ζ-potential. In general, flotation rate increases with increasing contact angle at all particle sizes. A higher froth height can result in a lower recovery but higher grade. In addition, increases in superficial gas rate and energy dissipation rate have beneficial

impacts on the flotation rate and recovery. The simulation results also suggest that a proper control of ζ-potentials helps increase the recovery of fine particles.

7. The first-principle flotation model has been used to simulate the performance of a flotation circuit that is similar to the Escondida copper flotation plant in Chile. In the present work, the effects of particle hydrophobicity (contact angle) and particle size control by re-grinding have been studied by simulation. The results show that the re-grinding of rougher-scavenger concentrate greatly increased the overall copper recovery, which can be attributed to the increased flotation rate with increasing surface liberation. The simulation results show also that an increase in contact angle by way of using a stronger collector greatly increased the copper recovery at the rougher flotation circuit. These results are consistent with the plant practice, demonstrating the benefits of using a first-principle flotation model/simulator to improve the performance of the real world flotation plants.

5.2 Recommendations for Future Research

Although the output from the flotation model fit the experiments data well and reasonably, they may not be sufficient. There are some assumptions and simplifications of flotation process in this flotation model, which can be improved by considering the following suggestions:

1. All of the model predictions made in the present work have been made using essentially a 'foam' model to account for the bubble coarsening effects. For industrial applications, however, it will be necessary to use a froth-phase recovery model that can predict the particle size and particle contact angles. Therefore, one should develop a more comprehensive model simulator using the froth model recently developed by Park and Yoon [36] to account for the particle effects on froth phase recovery.

2. In the present work, the values of particle ζ-potentials and bubble ζ-potentials are directly entered into the simulator by operators. In practice, these two parameters are difficult to measure. In order to make an easy-to-use flotation simulator, one should incorporate a simple model that can be used by operators predict the ζ-potentials built-in subprograms. It is possible to develop subprograms, because there is a wealth of information on such information in the literature.

3. Develop a model to evaluate probability of particle orientation during bubble-particle collision process in the pulp phase. In the current flotation model, one assumption is that each particle has a uniform surface, so that the particle hydrophobicity is the same everywhere on the particle surface, so is the contact angle. In reality, the particle surfaces are heterogeneous, not homogeneous. Therefore, it will be useful to develop a new probability model to describe the particle orientation when a particle collides with an air bubble. If an air bubble collides with the hydrophobic part of the particle surface, then the probability of bubble-particle attachment (P_a) will be high. While if an air bubble approaches to the hydrophilic part of the particle surface, then there is little possibility to form a bubble-particle aggregate in the pulp.

4. It will useful to extend the flotation model from a 2-component system a multi-component system. In the present work, only 2-types of minerals are considered, *e.g.*, chalcopyrite and silica. In flotation practice, however, more than one type of mineral may become hydrophobic upon collector addition. To cope with such a case, it may be useful to develop 3-component system, *e.g.*, copper-zinc flotation.

REFERENCES

1. Wills, B.A., *Wills' mineral processing technology: an introduction to the practical aspects of ore treatment and mineral recovery*. 2011: Butterworth-Heinemann.

2. Haynes, W., *British patent No. 488.* Feb. **23**: p. 1860.

3. Soni, G., *Development and Validation of a Simulator based on a First-Principle Flotation Model*. 2013, Virginia Tech.

4. Hines, P.R. and J. Vincent, *The early days of froth flotation*, in *Froth Flotation, 50th Anniversary Volume*. 1962, AIME New York. p. 11-38.

5. Lynch, A., et al., *History of flotation technology.* Fuerstenau, MC; Jamenson G. and Roe-Hoan Yoon. Froth flotation a century of innovation. SME, 2007: p. 65-91.

6. Welsby, S.D.D., *On the interpretation of floatability using the bubble load.* 2009.

7. Laskowski, J., *The relationship between floatability and hydrophobicity*, in *Advances in mineral processing: A half century of progress in application of theory and practive*. 1986.

8. Moys, M., *A study of a plug-flow model for flotation froth behaviour.* International Journal of Mineral Processing, 1978. **5**(1): p. 21-38.

9. Warren, L.J., *Determination of the contributions of true flotation and entrainment in batch flotation tests.* International Journal of Mineral Processing, 1985. **14**(1): p. 33-44.

10. Savassi, O., *Direct estimation of the degree of entrainment and the froth recovery of attached particles in industrial flotation cells*. 1999, University of Queensland.

11. Hay, M. and C. Rule, *SUPASIM: a flotation plant design and analysis methodology.* Minerals engineering, 2003. **16**(11): p. 1103-1109.

12. Guillaneau, J.-C., et al., *Simulation improvements in mineral processing.* Mineral Processing and Extractive Metallurgy Review, 1995. **15**(1-4): p. 205-216.

13. Villeneuve, J., J.-C. Guillaneau, and M.-V. Durance, *Flotation modelling: A wide range of solutions for solving industrial problems.* Minerals engineering, 1995. **8**(4): p. 409-420.

14. Kirjavainen, V., *Mathematical model for the entrainment of hydrophilic particles in froth flotation.* International journal of mineral processing, 1992. **35**(1): p. 1-11.

15. Do, H., *Development of a turbulent flotation model from first principles.* 2010.

16. Sherrell, I.M., *Development of a flotation rate equation from first principles under turbulent flow conditions*. 2004.

17. Sutherland, K., *Physical chemistry of flotation. XI. Kinetics of the flotation process.* The Journal of Physical Chemistry, 1948. **52**(2): p. 394-425.

18. Tomlinson, H. and M. Fleming. *Flotation rate studies*. in *Proceedings of the 6th International Mineral Processing Congress, Cannes*. 1965.

19. Yoon, R.-H. and L. Mao, *Application of extended DLVO theory, IV: derivation of flotation rate equation from first principles.* Journal of Colloid and Interface Science, 1996. **181**(2): p. 613-626.

20. Schubert, H., *On the turbulence-controlled microprocesses in flotation machines.* International journal of mineral processing, 1999. **56**(1): p. 257-276.

21. Abrahamson, J., *Collision rates of small particles in a vigorously turbulent fluid.* Chemical Engineering Science, 1975. **30**(11): p. 1371-1379.

22. Schulze, H.J., *Physicochemical elementary processes in flotation.* Elsevier Science Publishers, 1983, 1983: p. 348.

23. Lee, C.-H., L. Erickson, and L. Glasgow, *Bubble breakup and coalescence in turbulent gas-liquid dispersions.* Chemical Engineering Communications, 1987. **59**(1-6): p. 65-84.

24. Xu, Z. and R.-H. Yoon, *The role of hydrophobia interactions in coagulation.* Journal of Colloid and Interface Science, 1989. **132**(2): p. 532-541.

25. Yoon, R.-H. and S. Ravishankar, *Application of extended DLVO theory: III. Effect of octanol on the long-range hydrophobic forces between dodecylamine-coated mica surfaces.* Journal of colloid and interface science, 1994. **166**(1): p. 215-224.

26. Hogg, R., T. Healy, and D. Fuerstenau, *Mutual coagulation of colloidal dispersions.* Transactions of the Faraday Society, 1966. **62**: p. 1638-1651.

27. Rabinovich, Y.I. and N. Churaev, *Effect of electromagnetic delay on the forces of molecular attraction.* Kolloidnyi Zhurnal, 1979. **41**(3): p. 468-74.

28. Yoon, R.-H., D.H. Flinn, and Y.I. Rabinovich, *Hydrophobic interactions between dissimilar surfaces.* Journal of colloid and interface science, 1997. **185**(2): p. 363-370.

29. Pazhianur, R. and R.-H. Yoon, *Model for the origin of hydrophobic force.* Minerals & metallurgical processing, 2003. **20**(4): p. 178-184.

30. Goren, S.L. and M.E. O'Neill, *On the hydrodynamic resistance to a particle of a dilute suspension when in the neighbourhood of a large obstacle.* Chemical Engineering Science, 1971. **26**(3): p. 325-338.

31. Luttrell, G. and R.-H. Yoon, *A hydrodynamic model for bubble—particle attachment.* Journal of colloid and interface science, 1992. **154**(1): p. 129-137.

32. Levenspiel, O., *Chemical reaction engineering.* Industrial & engineering chemistry research, 1999. **38**(11): p. 4140-4143.

33. Narsimhan, G. and E. Ruckenstein, *Structure, drainage, and coalescence of foams and concentrated emulsions.* Surfactant Science Series, 1996: p. 99-188.

34. Leonard, R.A. and R. Lemlich, *A study of interstitial liquid flow in foam. Part I. Theoretical model and application to foam fractionation.* AIChE journal, 1965. **11**(1): p. 18-25.

35. Banisi, S. and J. Finch, *Technical note reconciliation of bubble size estimation methods using drift flux analysis.* Minerals Engineering, 1994. **7**(12): p. 1555-1559.

36. Park, S., *Modeling Bubble Coarsening in Froth Phase from First Principles*. 2015, Virginia Tech.

37. Sheludko, A., *Thin liquid films.* Advances in Colloid and Interface Science, 1967. **1**(4): p. 391-464.

38. Wang, L. and R.-H. Yoon, *Role of hydrophobic force in the thinning of foam films containing a nonionic surfactant.* Colloids and Surfaces A: Physicochemical and Engineering Aspects, 2006. **282**: p. 84-91.

39. Donners, W. and A. Vrij, *The critical thickness of thin free liquid films.* Colloid and Polymer Science, 1978. **256**(8): p. 804-813.

40. Vrij, A., *Possible mechanism for the spontaneous rupture of thin, free liquid films.* Discussions of the Faraday Society, 1966. **42**: p. 23-33.

41. Vrij, A. and J.T.G. Overbeek, *Rupture of thin liquid films due to spontaneous fluctuations in thickness.* Journal of the American Chemical Society, 1968. **90**(12): p. 3074-3078.

42. Pugh, R., *Foaming, foam films, antifoaming and defoaming.* Advances in Colloid and Interface Science, 1996. **64**: p. 67-142.

43. Welsby, S., S. Vianna, and J.-P. Franzidis, *Assigning physical significance to floatability components.* International Journal of Mineral Processing, 2010. **97**(1): p. 59-67.

44. Jameson, G.J., *The effect of surface liberation and particle size on flotation rate constants.* Minerals Engineering, 2012. **36**: p. 132-137.

45. Yianatos, J., L. Bergh, and G. Cortés, *Froth zone modelling of an industrial flotation column.* Minerals Engineering, 1998. **11**(5): p. 423-435.

46. Ahmed, N. and G. Jameson, *The effect of bubble size on the rate of flotation of fine particles.* International Journal of Mineral Processing, 1985. **14**(3): p. 195-215.

47. Chander, S. and D. Fuerstenau, *On the natural floatability of molybdenite.* Trans. AIME, 1972. **252**: p. 62-69.

48. Devivo, D.G. and B.L. Karger, *Studies in the flotation of colloidal particulates: effects of aggregation in the flotation process.* Separation Science, 1970. **5**(2): p. 145-167.

49. Reay, D. and G. Ratcliff, *Removal of fine particles from water by dispersed air flotation: effects of bubble size and particle size on collection efficiency.* The Canadian Journal of chemical engineering, 1973. **51**(2): p. 178-185.